Microphysical Characteristics of Super Typhoon Lekima (2019) and Its Impacts on Polarimetric Radar Remote Sensing of Precipitation

Yabin Gou[1, 2, 3], Haonan Chen[3], and Lulin Xue[4]

[1]Hangzhou Meteorological Bureau, Hangzhou 310051, China
[2]Zhejiang Institute of Meteorological Sciences, Hangzhou 321000, China
[3]Colorado State University, Fort Collins, CO 80523, USA
[4]National Center for Atmospheric Research, Boulder, CO 80307, USA

Corresponding author address: Haonan Chen (haonan.chen@colostate.edu)

Abstract. The complex precipitation microphysics associated with super typhoon Lekima (2019) and its potential impacts on the consistency of multi-source datasets and radar quantitative precipitation estimation has been disentangled using a suite of *in situ* and remote sensing observations around the disastrous waterlogging area near the groove windward slope (GWS) of Yan Dang Mountain and Kuo Cang Mountain, China. The dynamic microphysical processes, in which breakup overwhelms over coalescence as the main outcome of the collision of precipitation particles, noticeably changes the self-consistency between radar reflectivity (Z_H), differential reflectivity (Z_{DR}) and the specific differential phase (K_{DP}), and their consistency with theoretical counterparts simulated with surface disdrometer measurements, which are quality-controlled in terms of fall velocity characteristics of different hydrometeors to remove wind effects, hailstones and graupels. The overwhelming breakup accounts for phenomenon that high concentration rather than size contributes more to large Z_H of the storm and the large deviation of attenuation-corrected Z_{DR} from its expected values ($\hat{Z}_{DR}$). As a result, although a comparable performance of Z_H-based rainfall estimates $R(Z_H^C)$ and K_{DP}-based rainfall estimates $R(K_{DP})$ can be achieved, $R(Z_H, Z_{DR})$ tends to overestimate precipitation. $R(Z_H, \hat{Z}_{DR})$ performs the best among all rainfall estimators and it is less sensitive to the potential microphysical processes, owning to the improved self-consistency between radar-measured Z_H, Z_{DR} and K_{DP} and their consistency with surface counterparts.

Keywords: polarimetric radar; remote sensing of precipitation; quality-control; typhoon microphysics; extreme weather.

1. Introduction

Weather radars form the cornerstones of national weather warning and forecast infrastructure in many countries. In fact, Doppler radar network plays an indispensable role in modern meteorological and hydrological applications, such as quantitative precipitation estimation (QPE) in support of water resources management and flood prediction, especially during high-impact weather events in urban environments (Chandrasekar et al.,2018, Cifelli et al., 2018, Chen et al., 2018). Although the technical advances such as dual-polarization have tremendously improved weather radar applications in hydrometeorology remote sensing, it is still a challenge to incorporate complex precipitation dynamics and microphysics in an adaptive manner

to optimize the quantitative applications of polarimetric radar measurements, including horizontal reflectivity Z_H, differential reflectivity Z_{DR}, copolar correlation coefficient ρ_{HV}, differential propagation phase Φ_{DP} and its range derivative K_{DP} (specific differential phase). Traditional ways of using these measurements have only been able to extract part of the information due to the nature of the analytical tools and complex spatiotemporal variability of precipitation.

In general, there are three main factors contributing to radar QPE uncertainty: radar measurement error, parameterization error of various radar-rain rate (R) relationships, and random error. In practical applications, it is important to consider these three factors as a whole to make radar rainfall estimates approximate the true rainfall at surface as much as possible. Among conventional radar QPE algorithms, those developed based on Z_H measurements were typically used and are still in use today.
40 For instance, the earlier version of radar QPE algorithm in the National Oceanic and Atmospheric Administration (NOAA) Multi-radar Multi-Sensor System (MRMS) utilized multi-radar hybrid Z_H to derive radar-based rainfall field (Zhang et al., 2011). Recent update of MRMS incorporated the specific attenuation (A_H) and K_{DP} to enhance the Z_H-based algorithm (Wang et al., 2019) and such an update can benefit from (i) the insensitivity of A_H to raindrop size distribution (DSD) variability (Ryzhkov et al., 2014); (ii) K_{DP} is a better indicator of rain rate and liquid water content (LWC, g·m^{-3}) than Z_H since K_{DP} is more
45 tightly connected to the precipitation particle size distribution; (iii) $R(K_{DP})$ and $R(A_H)$ inherit the immunity of Φ_{DP} to miscalibration, attenuation, partial beam blockage, and wet radome effects (Park et al., 2005; Ryzhkov et al. 2014), which is hard to address when using Z_H for QPE, especially at higher frequencies such as C- and X-bands (Park et al., 2005; Matrosov.2010; Frasier et al., 2013). Multi-parameter radar QPE algorithms further integrates Z_{DR} with Z_H, K_{DP} or A_H to infer more information about raindrop shape, such as the double-measurement algorithm $R(Z_H, Z_{DR})$, $R(K_{DP}, Z_{DR})$, $R(A_H, Z_{DR})$ and
50 the triple-measurement radar QPE algorithm as $R(Z_H, Z_{DR}, K_{DP})$ (Matrosov,2010; Gosset et al., 2010; Schneebeli and Berne, 2012, Keenan et al., 2001; Chen et al., 2017; Gou et al.,2019), but these algorithms usually assume that Z_{DR} measurements are well calibrated and attenuation-corrected (Ryzhkov et al., 2005; Bringi et al., 2010).

In addition to radar measurements, disdrometer and rain gauge data are often used to determine the optimal radar-based QPE
55 algorithms (Lee and Zawadzki 2005; Tokay et al.,2005). For example, MRMS system utilizes long-term Z_H and gauge rainfall measurements to obtain climatological Z-R relationships for each precipitation type (Zhang et al., 2011). In Gou et al. (2018, 2020), rain gauge measurements are used to dynamically adjust Z-R relationships to effectively reflect the evolution of precipitation systems. Nevertheless, the accuracy of meteorological gauge rainfall recordings is usually configured as 0.1 mm, rain gauge may record less rainfall than reality due to the quickly spinning of tipping bucket in heavy shower situations. In
60 addition, the surface wind may hinder some raindrops from falling into the tipping bucket, and the mechanical failures of the tipping bucket will record abnormally high or low rainfall, which introduces significant errors to gauge network. Similarly, disdrometer measurements can be affected by strong winds and mixed-phase hydrometeors falling through the laser sampling area of the disdrometer, resulting in degraded quality of the DSD recordings (Tokay and Bashor, 2010). Since the DSD data

collected by disdrometers are indispensable and sometimes are the only resources that can be used for precipitation
65 microphysical analysis and the establishment of polarimetric radar rainfall relationships, meticulous quality control (QC) must
be done on the disdrometer measurements (Friedrich et al., 2013; Gou et al., 2021).

Another issue that is important but rarely considered in radar QPE is the changing microphysics occurred during the falling
processes of precipitation particles between radar range volumes and surface ground, which is often indicated by the
70 inconsistent radar observations with their surface counterparts. The Z_H measurements in the melting layer (ML) of a stratiform
rain system, which is featured by falling melting snowflakes or ice crystals, usually need to be corrected for bright band for
subsequent rainfall retrievals, especially when little rain is reported on the ground (Chen et al., 2020). The severe updraft
accompanied in a convective storm shower may introduce large Z_H and Z_{DR} column (Snyder et al., 2015; Carlin et al., 2017),
while surface rain gauge may record little or time-lagged rainfall, which is frequently perceived in the front of the squall line
75 system or wind gust system. In addition, the contamination on K_{DP} and A_H from mixed-phase hydrometeor particles may make
$R(K_{DP})$ and $R(A_H)$ overestimated (Gou et al., 2019), and the falling hailstones may also contaminate radar measured Z_H, K_{DP}
and A_H (Donavon and Jungbluth, 2007; Ryzhkov et al., 2014), leading to an overestimated hotspot on the derived rainfall field
if such contaminations are not well addressed.

80 The complex microphysical variations mentioned above may exist in different precipitation events or even coexist in a large-
scale precipitation system such as typhoon. This paper focuses on the most disastrous area caused by Super Typhoon Lekima
(2019) landing on the coast of Zhejiang province of China, and investigates the complicated microphysical characteristics of
the typhoon-induced storm after its landing and their impacts on multi-source data consistency and polarimetric radar QPE
performances, using observations from a S-band polarimetric radar deployed at Wenzhou (hereafter referred to as WZ-SPOL)
85 and measurements from six Thies disdrometers and a local rain gauge network around the disastrous area. It was the most
destructive landing typhoon during 2019 in China and the third strongest typhoon in the history of Zhejiang since 1949. So far,
the reason for the significant convective asymmetries in the concentric eyewalls before its landing, which was ascribed to
phase locking of vortex Rossby waves (VRW), and the cloud and precipitation microphysics caused by this phase-locking
VRW-triggered asymmetric convection have been respectively revealed (Dai et al. 2021; Huang et al. 2022), mainly based on
90 the WZ-SPOL radar and another Doppler weather radar at Taizhou (TZ). The DSD characteristics in the eyewall and spiral
rainbands based on surface disdrometer measurements have also been demonstrated (Bao et al., 2020). However, the unique
microphysical processes inherent in typhoon after its landing have not been thoroughly investigated.

The novel contributions of this paper are summarized as follows: 1) An enhanced QC procedure for disdrometer measurement
95 is developed and analyzed through cross-comparison with rain gauge and WZ-SPOL radar measurements. 2) The impacts of
dynamic precipitation microphysical process on the consistency between radar, gauge, and disdrometer measurements are

thoroughly investigated, and the microphysical information is incorporated in deriving optimal radar QPE. 3) This paper proposes a unique $R(Z_H, Z_{DR})$ estimator, which integrates the expected Z_{DR} (i.e., $\hat{Z}_{DR}$) estimated from attenuation-corrected Z_H (i.e., Z_H^C) to mitigate the negative effects brought by the special microphysical processes.

100

The remainder of this article is organized as follows: Section 2 introduces the study domain, hardware configuration and data processing methodologies. Section 3 details the precipitation microphysics associated with Lekima (2019) and its impacts on the consistency between multi-source data. The radar QPE performance before and after incorporating the dynamic precipitation microphysics is also quantified in Section 3. Section 4 summarizes the main findings of this study and suggests

105 future directions in implementing this work in operational environment.

2. Study Domain and Data Processing

2.1. Study Domain

As shown in Fig. 1a, this paper focused on the north side of WZ city and south side of TZ city. These two cities are both regional central cities: WZ is an important trade city and TZ is an important seaport city in southeastern China. Typhoon landed

110 on the coastline of these two cities most frequently in history, indicating the necessity and importance to monitor typhoons coming into this area. For this aim, the S-band weather radar in WZ was upgraded to a polarimetric radar system in 2019 to enhance its precipitation monitoring capability. WZ-SPOL radar is deployed on a mountain near the coastline as depicted in Fig. 1a, and it well covers the flood and waterlogging disaster area caused by the landfall of super typhoon Lekima (2019). Two mountains lay between WZ and TZ, Kuo Cang Mountain (KCM) and Yang Dang Mountain (YDM), although the

115 mountainous terrain causes no serious beam blockage of WZ-SPOL radar. In addition, KCM and YDM are both featured with a typical groove topography as indicated by the dashed lines in Fig. 1a, which benefits assembling and uplifting of water vapor on the lower atmospheric layers.

Six Thies laser-optical disdrometers have been deployed at the national meteorological stations around the target area since

120 2017 (see Figs. 1a and 1b), which includes Xian Ju (XJ), Lin Hai (LH), Win Ling (WL), Hong Jia (HJ), Yu Huan (YH) and Dong Tou (DT), and they can provide of hydrometeor particle size and falling velocity (diameter-velocity) measurements with a one-minute time resolution. These diameter-velocity measurements are utilized to calculate rainfall intensity and to simulate dual-polarization radar measurements near the surface.

125 In addition, 356 tipping-bucket rain gauge stations (see Fig. 1b) are uniformly deployed around 10 towns, which suffered from landslide and waterlogging disasters within the coverage of radius of 135 km from the WZ-SPOL radar. The time resolution

of the gauge measurements is also configured as one minute and only gauge observations without any interruptions are utilized in this study. A removal operation on gauge measurements is done if the gauge measurement record is suspected to be false report when the ratio between any radar hourly rainfall estimates (detailed in 3.3) exceeds 10. This operation attempts to
130 eliminate outliers from gauge rainfall recordings.

Typhoon Lekima (2019) landed on the coastal area of Chengnan town in WL city at 1745 UTC, 9 August 2019 and the maximum wind near its center was about 52 m·s^{-1}, which made it the strongest typhoon landing China in 2019 and the third strongest landing typhoon in history of Zhejiang since 1949. According to the statistics, its influenced area with rainfall
135 measurements over 100 mm was about 361000 square kilometers and the daily rainfall at 19 national stations had broken their historical records. During the landfall, high waves were stirred up along the coastline as depicted in Fig. 2a, and the landslide in Fig. 2b blocked the river and temporally formed a dyke with a sudden rose of water level of the river before the collapse of the landslide dyke, resulting in 22 casualties around this area. The waterlogging submerged the road network and many buildings in the urban area of WL, LH, YH and XJ in TZ city (see Figs. 2c-2f). Millions of people evacuated from TZ city or
140 were trapped in the disaster area. A total of 57 casualties were reported due to the landslides, flood or waterlogging during the landfall of Lekima (2019).

2.2. Radar Configuration and Data Processing

The simultaneous horizontal and vertical polarization mode is adopted by the WZ-SPOL radar. For the routine operations, the standard volume coverage pattern (VCP21) is configured, which has elevation angles, including 0.5°, 1.5°, 2.4°, 3.3°, 4.3°, 6.0°,
145 9.9°, 14.5° and 19.5°. The azimuthal radial resolution is set as 0.95° and the range gate resolution is configured as 250m for all elevation angles. Radar-measured Z_H, Z_{DR}, ρ_{HV}, radial velocity (V_R), and Ψ_{DP} are archived into a ".bz2" package in the radar data acquisition (RDA) system and then transferred to radar products generation system to produce some predefined standard radar products. QC processing for WZ-SPOL radar data is performed using the following steps:
(i) Ground clutter (GC) identification and mitigation.
150 Two parts are included in this step. The clutter mitigation decision (CMD) algorithm (Hubbert et al. 2009) has been integrated into the RDA software to filter the ground clutters in real time, but some residual static ground clutters (RSGC) still exist in the WZ-SPOL radar measurements at 0.5° elevation angle. To further eliminate the RSGC, WZ-SPOL radar Z_H measurements at 0.5° elevation angle during August of 2019 are utilized. The max number (N_{max}) of the pixel with $Z_H>0$dBZ within 55 km from the WZ-SPOL radar is 6981 and the observation number (N_{obs}) of each pixel within this range is normalized by dividing
155 N_{max}. Then, a RSGC statistical map is derived as shown in Fig. 3a, which represents the relative frequency (Freq. % of $Z_H>0$dBZ) within the coverage of WZ-SPOL radar. In this map, the pixels with Freq>50% are deemed to be contaminated by the RSGC and they form a RSGC mask in Fig. 3b to eliminate RSGC-contaminated Z_H and Z_{DR} at the 0.5° elevation angle of the WZ-SPOL radar.

160 (ii) Ψ_{DP} processing

A nine-gate smoothing is first carried out to suppress the noise signals along the Ψ_{DP} range profile. Then, a Ψ_{DP} dealiasing procedure is executed to correct the aliased Ψ_{DP} based on the standard deviation of Ψ_{DP} in nine consecutive range gates (Wang et al., 2009) and 360° is added on the aliased Ψ_{DP} to guarantee a monotonically increasing Ψ_{DP} range profile. In addition, the iterative filtering method in Hubbert and Bringi (1995) is used to filter the backscatter differential phase, and a zero-started

165 filtered Φ_{DP} (Φ_{DP}^{filter}) range profile is obtained by removing the initial phase of Φ_{DP}. The Φ_{DP}^{filter} range profile is utilized to estimate K_{DP} through a linear fitting approach (Wang et al., 2009) with additional non-negative constraint on K_{DP}.

(iii) Attenuation correction for Z_H

The ZPHI method proposed by Bringi et al. (2001) is extended for correcting S-band Z_H measurements.

170
$$A_H(r) = \frac{[Z_H^M]^b[10^{0.1b\alpha\Delta\Phi(r_0,r_m)}-1]}{I(r_0,r_m)+[10^{0.1b\alpha\Delta\Phi(r_0,r_m)}-1]I(r,r_m)} \tag{1a}$$

$$\Delta\Phi_{DP}(r_0,r_m) = \Phi_{DP}(r_m) - \Phi_{DP}(r_0) \tag{1b}$$

$$I(r_0,r_m) = 0.46b \int_{r_0}^{r_m}[Z_H^M(r)]^b dr \tag{1c}$$

$$I(r,r_m) = 0.46b \int_{r}^{r_m}[Z_H^M(r)]^b dr \tag{1d}$$

$$\Phi_{DP}^{rec}(r_0,r_m) = \int_{r_0}^{r_m} \frac{A_H(s,\alpha)}{\alpha} ds \tag{1e}$$

175
$$C(r_0,r_m) = \int_{r_0}^{r_m}|\Phi_{DP}^{rec}(s,\alpha) - \Phi_{DP}| ds \tag{1f}$$

$$Z_H^C(r) = Z_H^M(r) + 2\int_{0}^{r} A_H(s,\alpha) ds \tag{1g}$$

where Z_H^M and Z_H^C denote the measured and attenuation-corrected reflectivity, respectively; Φ_{DP} refers to filtered differential phase; Φ_{DP}^{rec} is reconstructed differential phase through the ZPHI processing chain with an optimal coefficient α iteratively searched in the range [0.01, 0.12] by step 0.01 until the cost function $C(r_0,r_m)$ of the difference between Φ_{DP} and Φ_{DP}^{rec} in Eq.

180 (1f) is minimized. The coefficient b is assumed as a constant 0.62 for S-band (Ryzhkov et al.,2014).

The ZPHI method utilizes Z_H^M and $\Delta\Phi_{DP}$ in Eq. 1b to calculate attenuation A_H. Here, it should be noted that three constraints are imposed on the ZPHI processing chain to ensure the practical performance, including non-negative constraint on A_H, ρ_{HV} constraint on the range gates partitioning, and convergence constraint to avoid incorrect calculation termination (Gou et al.,

185 2019). Finally, Z_H^M is corrected as Z_H^C according to Eq. 1g.

(iv) Z_{DR} processing

The Z_{DR} offset can be obtained with respect to the nearly zero values of Z_{DR} in the light rain scenarios and then this offset is applied to make sure the Z_{DR} bias is small. In addition, the exponential Z_{DR}–Z_H relationship is established as Eq. 2a based on

190   quality-controlled DSD dataset detailed in Section 2.3 and the analysis in Section 3.1. Therein, Z_H, Z_{DR} and K_{DP} are simulated

using the T-matrix method, assuming the raindrop aspect ratio in Brandes et al. (2002) at temperature of 20°C. Then, the

differential attenuation factor (A_{DP}) in Eq. 2b is calculated through adjusting β to obtain potential Z_{DR}^C calculated according to

Eq. 2c. The optimal β can be iteratively determined for A_{DP} by minimizing the differences between Z_{DR}^C and $\hat{Z}_{DR}$ in Eq. 2d,

along the whole radial range profile. In this process, additional ΔZ_{DR} is also iteratively imposed on the whole range profile

195   with step as 0.1 dB to mitigate the residual Z_{DR} bias caused by miscalibration or wet radome effects. Then, Z_{DR}^M is corrected by

Eq. 2c as Z_{DR}^C through A_{DP} calculated by the optimal β. Z_{DR}^C is utilized for the subsequent analysis and radar rainfall estimation.

$$\hat{Z}_{DR}(r) = 2.1062 \times 10^{-5} Z_H^C(r)^{2.9151} \qquad (2a)$$

$$A_{DP}(r; \beta) = \frac{\beta}{\alpha_{opt}} A_H(r; \alpha_{opt}) \qquad (2b)$$

$$Z_{DR}^C(r; \beta) = \Delta Z_{DR} + Z_{DR}^M(r) + 2\int_0^r A_{DP}(s, \beta)ds \qquad (2c)$$

200    $$C_{DR}(r_0, r_m) = \int_{r_0}^{rm} \left| Z_{DR}^C(r; \beta) - \hat{Z}_{DR}(r) \right| dr \qquad (2d)$$

2.3. DSD Data Processing

The Thies disdrometer diameter-velocity measurements configured with 1-min sampling intervals collected during the period

between 0000 UTC, 09 August 2019 and 0000 UTC 11 August 2019 are utilized. Nearly all the diameter-velocity

measurements from the six national meteorological stations were affected by the strong winds with the hourly maximum wind

205   speed larger than 20 m·s^{-1} as depicted in Fig. 4. In particular, YH, WL and DT are affected more seriously with their hourly

maximum wind speed exceeding 40 m·s^{-1} after 1600 UTC, 09 August 2019. Theoretically, the diameter–velocity measurements

of raindrops should be uniformly distributed as the drop velocity model in Beard (1977), which can be represented as

$$V_B(D_i) = 9.65 - 10.3 \times e^{-0.6D_i} \qquad (3)$$

where D_i is the diameter of i_{th} size class (diameter interval) and V_B is estimated by D_i. However, real velocity measurement

210   (V_M) of disdrometers may deviate seriously from V_B due to the strong wind effects. For instance, many diameter-velocity

measurements at all six stations are biased with $V_M < 0.5 V_B$ and distributed in all predefined size class; more deviated velocity–

diameter measurements of WL, YH and DT are featured with $V_M < 0.5 V_B$ in Figs. 5d, 5e and 5f than that of XJ, LH and HJ in

Figs. 5a, 5b and 5c, which can be ascribed to stronger wind speeds, too. Consequently, these disdrometer measurements need

to be preprocessed and the QC procedure utilized hereafter include the following three steps:

215   (i) For wind contaminated diameter–velocity measurements, if V_M of the i_{th} size class is located inside $[0.5V_B, 1.5V_B]$

(enclosed by the blue lines in Fig. 5), the diameter-velocity measurements are deemed to agree well with Eq. 3 and would be

kept;

(ii) For the potential hail ($D_i > 5$mm) and graupel (D_i in [2mm, 5mm]), two diameter–velocity relationships listed in

Friedrich et al. (2013) as

220
$$V_{\mathrm{H}}(D_i) = 12.43 \times (0.1D_i)^{0.5} \tag{4a}$$
$$V_{\mathrm{G}}(D_i) = 1.3 \times (0.1D_i)^{0.66} \tag{4b}$$

are selected to estimate the velocity of potential hail (V_{H}) and lump graupel (V_{G}) corresponding to D_i. If $|V_{\mathrm{B}} - V_{\mathrm{M}}| < |V_{\mathrm{H}} - V_{\mathrm{M}}|$ or $|V_{\mathrm{B}} - V_{\mathrm{M}}| < |V_{\mathrm{G}} - V_{\mathrm{M}}|$ is determined, it indicates the diameter–velocity measurements are more prone to raindrops and they are kept; otherwise, these measurements are also eliminated from the original dataset depicted in Fig. 5.

225

(iii) For the residual contaminations which cannot be directly eliminated by the abovementioned processing due to their similar diameters to raindrops, another analysis based on DSD-derived median volume diameter (D_0) and Z_{DR} are utilized. Because larger Z_{DR} values are anticipated for wet hail and graupel than raindrops with similar diameters. The final QC processing result of DSD dataset is presented in Section 3.1.

230 **3. Analysis and Results**

3.1 The consistency between multi-source data

3.1.1 The consistency between disdrometer and rain gauge measurements

DSD measurements are important basis to establish some necessary relationships between polarimetric radar variables for radar QPE algorithms. However, DSD-derived rainfall recordings, which are directly calculated from the diameter-velocity
235 measurements in Fig. 5 without any QC processing, all presented unrealistic values. An alternative representation of DSD-derived rainfall (i.e., R_{DSD}) can be represented as

$$R_{\mathrm{DSD}} = \begin{cases} R_{\mathrm{T}} + (R_{\mathrm{M}} - R_{\mathrm{T}})/C_{\mathrm{T}} & R_{\mathrm{M}} > R_{\mathrm{T}} \\ R_{\mathrm{M}} & R_{\mathrm{M}} \leq R_{\mathrm{T}} \end{cases} \tag{5}$$

where R_{M} stands for DSD-derived rainfall without any transform; R_{T} stands for a rainfall threshold which is larger than the maximum gauge-measured rainfall; DSD-derived rainfall exceeding R_{T} is divided by a constant coefficient C_{T} to shrink this
240 part into a limited range interval in Fig. 6. C_{T} indicates that DSD-derived rainfall without QC processing is at least C_{T} times higher than the one after QC processing.

Accordingly, the maximum hourly rainfall at LH, XJ and HJ exceeded 200 mm, that at DT exceeded 400 mm, and that at WL and YH unbelievably exceeded 3×10^3 mm and 10^4 mm during Lekima (2019). C_{T} of these stations in Fig. 6 indicates that
245 they are at least 20 times and at most 800 higher than gauge-measured rainfall recordings. Meanwhile, DSD-derived maximum Z_{H}, Z_{DR}, K_{DP} and R respectively exceeded 85dBZ, 5.5dB, 1500deg·km^{-1} and 15000mm/h (see Figs. 7a-7c), and they are extremely higher than the final QC-processed counterparts (rectangle in Figs. 7a-7c). If these unrealistic DSD-derived variables are directly utilized to establish the parameters of any radar QPE algorithm, unrealistically overestimated radar rainfall field

will be obtained. Therefore, the QC procedure in Section 2.3 is first imposed on the DSD dataset, and its performance and
250 effectiveness are investigated through the comparison with gauge-measured rainfall recordings.

According to visual comparison of hourly rainfall timeseries in Fig. 6, the serious overestimation of DSD-derived rainfall
recordings at all six stations are largely reduced after the removal of particles caused by wind contaminations by eliminating
the diameter-velocity measurements with V_M outside $[0.5V_B,1.5V_B]$. It is also noticed that DSD-derived rainfall timeseries have
255 begun to approximate to gauge-measured rainfall timeseries of XJ, HJ and LH in Figs. 6a-6c, and the further hail and graupel
processing hardly changes these DSD-derived rainfall timeseries, indicating the contamination of hail or graupel are not serious
at these three stations.

In contrast, DSD-derived rainfall timeseries at the other three stations performs oppositely. DSD-derived rainfall timeseries at
260 WL presents nearly complete consistency with its gauge-measured rainfall recordings after processing the hail contaminations
but underestimated after processing some graupel contaminations (see Fig. 6d). It implies that WL suffers some contamination
of hail and graupel at the same time, but some graupel particles may have similar diameters with raindrops which can be called
raindrop-like graupel particles. It indicates the existence of some raindrop-like graupels and the removal of them is responsible
for the DSD-derived rainfall underestimation of WL after QC processing, and some other raindrop-like graupels might be kept
265 if this underestimation is reasonable. Furthermore, YH suffers more contaminations from graupel than hail. During its peak
rainfall recording period between 1600 UTC and 2200 UTC, 09 August 2019 in Fig. 6e, DSD-derived rainfall at YH changes
relatively less after processing hail but still deviates largely from gauge-measured rainfall, however, better approximation as
well as an overall underestimation can be perceived after graupel processing. It indicates that some raindrops might be
identified as graupels or some graupels might completely melt as raindrops and then measured by gauge tipping bucket, and
270 radar and disdrometer comparison (in 3.1.2) favor the former more than the later possibility. DT suffer less hail and graupel
contamination than WL and YH, but more than XJ, HJ and LH, therefore, its DSD-derived rainfall timeseries in Fig. 6f changes
just a little after further hail and graupel processing compared with the gauge rainfall timeseries.

In general, DSD-derived rainfall at WL, YH and DT all exhibit an overall underestimation tendency compared with gauge
275 rainfall series after processing hail and graupel contamination. Some melt raindrop-like graupels into the tipping bucket can
account for these underestimates; Conversely, if these QC processing cannot eliminate all hail or graupel particles, these
residual solid particles could result in a false relationship between D_0 and Z_{DR}.

As shown in Fig. 8a, the fitted curve uniformly passed through the scattergram and it apparently represents a good fitting
280 relationship between D_0 and Z_{DR}. However, as abovementioned, these DSD-derived D_0 and Z_{DR} still suffer some hail and
graupel contaminations after processing the wind effects. Even after processing hail and graupel contaminations, the

scattergram in Fig. 8b still presents an obviously overfitted relationship between D_0 and Z_{DR}, where exists a clear boundary with $Z_{DR}>2.5$dB, and they can be caused by wet hailstones or graupels with D_0 ranging from 1.5 mm to 4 mm and some of them has raindrop-like size (<2mm). Finally, DSD-derived variables constrained by $Z_{DR}<2.5$dB are assumed to represent pure

285 raindrops near the surface, and they are finally utilized to fit the relationships between polarimetric variables, such as the D_0-Z_{DR} relationship in Fig. 8c, LWC-K_{DP} relationship in Fig. 8d and K_{DR}-Z_H relationship in Fig. 8e, as well as the Z_{DR}-Z_H relationship in Eq. 2a (see Fig. 8f).

$$D_0 = 0.2987 \times Z_{DR}{}^3 - 1.3229 \times Z_{DR}{}^2 + 2.1931 \times Z_{DR} + 0.3543 \quad (6)$$

$$\text{LWC} = 2.0949 \times K_{DP}^{0.6889} \quad (7)$$

290 $$K_{DP} = 1.5473 \times 10^{-13} \times Z_H^{8.8365} \quad (8)$$

Combining these relationships and another relationship between the normalized concentration of raindrops (N_w), LWC and the mean volume diameter of the drop size distribution (D_m) as:

$$N_w = \frac{4^4}{\pi \rho_w} \frac{\text{LWC}}{D_m^4} \quad (9)$$

$$D_m = \frac{4+\mu}{3.67+\mu} D_0 \quad (10)$$

295 where ρ_w is the water density (1 g·cm^{-3}). Based on Eqs (6)-(10), high resolution DSD parameter fields can be derived from WZ-SPOL radar measurements.

3.1.2 The consistency between radar and disdrometer measurements

The self-consistency between radar variables and the consistency between radar and DSD measurements need to be presented in advance to demonstrate the credibility of DSD-derived and radar-measured Z_H, Z_{DR} and K_{DP} through scattergrams and

300 timeseries comparison in Figs. 9 and 10. The scattergrams in Figs. 9b and 9d are derived from all Z_H^C, Z_{DR}^C and K_{DP} measurements described in Fig. 11. The ZHPI method (Bringi et al.2001) with more constraints described in Gou et al. (2019) effectively mitigates the attenuation effects on Z_H and Z_{DR} of the WZ-SPOL radar. The spatial fields of Z_H^M and Z_{DR}^M are not presented (they will not be used for the subsequent analysis) but it is easy to notice that radar-measured Z_H^M, Z_{DR}^M and K_{DP} are not self-consistent before attenuation correction processing: it is prominent for $Z_H^M>40$dBZ and $K_{DP}>1$deg·km^{-1} that K_{DP}-Z_H^M

305 scatters deviates positively from the theoretical K_{DP}-Z_H curve (Eq. 8 as depicted in Fig. 8e), and larger Z_H is anticipated for the these K_{DP} measurements. In addition, an overall deviation of Z_{DR}^M-Z_H^M distribution in Fig. 9c from their theoretical Z_{DR}-Z_H curve (Eq. 2a as depicted in Fig. 8f) addresses the coexistences of negative Z_{DR} bias and differential attenuation. In contrast, the scattergram core areas in Figs. 9b and 9d (defined as $\log_{10}(N)>2$) are featured with reduced density but more compact K_{DP}-Z_H^C distribution along theoretical K_{DP}-Z_H and Z_{DR}-Z_H curves, it conversely demonstrates that some Z_{DR}^M and Z_H^M are indeed

310 simultaneously corrected as larger Z_H^C and Z_{DR}^C values, therefore reducing the density at coordinates with smaller Z_H^C and Z_{DR}^C. Resultantly, the self-consistency between Z_H^C, Z_{DR}^C and K_{DP} is enhanced, meanwhile, these radar measurements become more consistent with their DSD-derived counterparts in terms of their referenced K_{DP}-Z_H and Z_{DR}-Z_H curve. Even though, serious

underestimation (≈-0.5 dB) of Z_{DR}^{M} and Z_{DR}^{C} still exist particularly when the corresponding reflectivity is larger than 35 dBZ (rectangular area in Figs. 9c and 9d), which is likely due to that larger-sized raindrops are observed near the surface.

315

In addition, enhanced self-consistency between Z_{H}^{C}, Z_{DR}^{C} and K_{DP} does not mean that WZ-SPOL radar measurements could absolutely agree with their DSD-derived counterparts near the surface. The time series in Fig. 10 shows that extremely large DSD-derived Z_H, Z_{DR} and K_{DP} in Fig. 7 (timeseries not presented) has absolutely diminished after QC processing wind effects, it conversely reflects that they are far larger than its WZ-SPOL radar counterparts before QC processing. In fact, DSD-derived

320   Z_H, Z_{DR} and K_{DP} timeseries begin to present a similar evolution tendency to their radar-measured counterparts after processing the wind effects. The further processing of hails and graupels makes them become overall more consistent with radar measurements at all stations, however some residual differences of DSD-derived Z_H, Z_{DR} and K_{DP} are still large at WL and YH in some time frames in Fig. 10, reflecting some uncertain but potential dynamic microphysical process: (i) WZ-SPOL radar measured larger Z_H and K_{DP} but similar Z_{DR} to DSD-derived counterparts at WL station (in rectangle 1) and it is associated

325   with the severe updraft accompanied with typhoon landing, more concentrated hydrometeors aloft than the surface are observed in this process. (ii) The following reversed situation (in rectangle 2) is smaller radar-measured Z_H, K_{DP} and Z_{DR} than their DSD-derived counterparts. This is due to the falling hails and graupels following the severe updraft (before they are eliminated). Even after eliminating hail and graupels, some raindrop-like graupels remained (Z_{DR}<2.5dB in Fig.8c) and this is verified by the underestimation of DSD-derived rainfall after final QC processing process (WL in Section 3.1.1). These residual

330   graupels might completely melt into large raindrops, which also contributes to large Z_{DR}. (iii) Another situation (in rectangle 3) is that radar measured larger Z_H and K_{DP} but smaller Z_{DR} than disdrometer after hail and graupel processing. Some raindrops might be mixed with raindrop-like graupels and were eliminated in the QC procedure, which is indicated by the higher DSD-derived rainfall than gauge measured rainfall after hail processing but slightly lower rainfall after further graupel processing (YH in Section 3.1.1), which corresponds to the larger/smaller DSD-derived counterparts before/after hail and graupel

335   processing. Besides, some more complicated dynamic microphysical processes coexisted during typhoon landing and evolution.

3.2 Microphysical characteristics of Lekima (2019)

When Super Typhoon Lekima (2019) landed on the eastern coast of China, several beneficial conditions for its evolution can be perceived: (i) KCM and YDM located in the way of typhoon brought serious interaction with landing typhoon; (ii) the wind

340   speed shear (the bold black curves in Figs. 11a-11d) with obvious V_R differences benefited the strengthening development of convective storms accompanying with Lekima; (iii) Lekima carried abundant warm moistures which can condensate easily if confronted with cold air.

The apparent characteristics of Lekima (2019) can be simply described based on Z_H: the outer and inner eyewalls were both

345 featured with Z_H>55dBZ before the landfall in Fig. 11e, indicating the enhanced convective development of the concentric eyewalls before its landing; after landing, the inner eyewall destructed and merged with the outer eyewall into a huge storm with enlarged area with Z_H>55dBZ enlarged around the GWS of YDM (in Fig. 11f), and then storm area with Z_H>55dBZ transitioned to the north GWS of YDM (in Fig. 11g) but gradually weakened when it passed over the mountain ridge between YDM and KCM (as depicted Fig. 11h). Other than this simple description, complex precipitation microphysical processes

350 accompanied with Lekima exhibited several external phenomena, which needs to be exploited by combining Z_{DR} and K_{DP} as well as the other radar-retrieved variables, such as $\hat{Z}_{DR}$ calculated through Eq. 2a based on Z_H^C and DSD parameter spatial fields in Fig. 13.

A nonnegligible phenomenon is associated with the microphysical composition of the storm. It could be visually perceived

355 that Z_{DR}^C in Figs. 11i-11l underestimated largely compared with $\hat{Z}_{DR}$ in Figs. 11m-11p in areas with significant K_{DP} in Figs. 11q-11t. Apparently, Z_{DR}^C cannot completely approximate to $\hat{Z}_{DR}$ through attenuation correction; intrinsically, the microphysical composition noticeably changes the Z_H-Z_{DR}-K_{DP} distribution within the storm. One typical radial range profile in Fig. 12 is detailed to make it clear. The storm in the ellipse-surrounded area in Figs. 12a and 12b contributes most attenuation and differential attenuation with maximum ΔZ_H=7.9dBZ and ΔZ_{DR}=0.645dB respectively at range 200km. Although the

360 correction can make enhanced consistency between Z_H and K_{DP} (see Section 3.1.2) and some Z_{DR}^C have indeed approximated well to $\hat{Z}_{DR}$ (outside the ellipse), the other Z_{DR}^C within the storm (ellipse-surrounded gates) still have a residual Z_{DR} bias about -1dB. Additionally, ρ_{HV} ranging from 0.99 to 1 (in Fig. 12c) further indicates the dominance of pure liquid raindrops (warm rain process); high LWC and N_w can be deduced respectively according to Eqs. 8 and 9 from K_{DP} ($\approx$3.5deg·km^{-1}; $\Delta\Phi_{DP}\approx$68.5 deg in Fig. 12c). Considering that Z_H is a composite integral of hydrometeors with different size and concentration but Z_{DR} is

365 less sensitive to little-sized raindrops, high concentration other than large size contributes more to the large Z_H^C, this composition resultantly causes overestimated $\hat{Z}_{DR}$ and inconsistent Z_H-Z_{DR}-K_{DP} distribution of WZ-SPOL radar measurements.

One dynamic microphysical process for this inconsistency is the hydrometeor size sorting (HSS). It externally exhibits the inconsistent positions of large Z_{DR} values and the maximum Z_H and K_{DP} within a storm. This was significant in the inner

370 eyewall (ellipse-surround area in Figs. 11e, 11i and 11q) and consequently large $\hat{Z}_{DR}$ horizontally deviated from large Z_{DR} in the downwind of rotational flow of inner eyewall and similar outward position deviation existed in the outer eyewall (in Fig. 11m) when the outer eyewall of Lekima crossed the coast near WL. HSS is usually caused by the differential sedimentation of hydrometeors with various sizes. Here the exhibition D_0>1.8 mm (in Fig.13a) as well as high LWC (>3 g·m^{-3} in Fig. 13e) but relatively lower $\log_{10}(N_w)$ in the large Z_{DR}^C area (<4.4 m^{-3}·mm^{-1} in Fig. 13i) indicated the dominant low-density large-sized

375 hydrometeors, such as big raindrops, graupels or hailstones. The accretion process dominated above the ML benefited generating large-sized graupels. But below the ML (warm rain environment), completely melted ices or graupels will transform into big raindrops; partly melting graupels will continue increasing their size, some transform into large-sized hailstones and

the others will directly fall on the ground, which has been verified through the comparisons at WL as discussed in 3.1. In addition, the highest hydrometeor concentration area with $\log_{10}(N_w)>4.4$ m$^{-3}\cdot$mm^{-1} dwelled on the southwestern outward

380   rainband of the outer eyewall dominated by $D_0<1.625$ mm, attributing to the advection by the strong tangential winds. However, HSS cannot account for the overall underestimation of Z_{DR} when the positions with large Z_H, Z_{DR} and K_{DP} values coincide with each other.

Another dynamic microphysical process is associated with the collision process in warm rain. There are three probable

385   colliding outcomes of collision process, bounce, coalescence, and breakup. Coalescence boosts increasing but breakup leads to decreasing the raindrop size. The existences of large raindrops with $D_0>1.8$ mm (in Figs. 13b and 13c) indeed back the collision-coalescence processes, which corresponds to Z_{DR} (>1.8 dB in Figs. 11j and 11k), and the coupling melting graupels may further favor this size increase (in Figs. 11a and 13a). However, the size increases contribute relatively little to Z_H^C, which causes abovementioned overestimated $\hat{Z}_{DR}$ for Z_{DR}^C. In contrast, raindrop collision-breakup conversely favors increasing

390   concentration of little-sized raindrops in one range gate. Colliding bounce cannot change raindrop size and concentration in a limited domain, but bouncing raindrops may collide with the other raindrops shortly in a highly concentrated warm rainstorm. Hence, breakup overwhelms coalescence as the main outcome, which can effectively account for the prevalent large Z_{DR}^C deviation (Fig. 11) from $\hat{Z}_{DR}$ and the abovementioned more significant contribution of raindrop concentration than size to Z_H^C.

395   However, a dynamic microphysical balance between coalescence and breakup was certainly achieved during the evolution of typhoon. D_0, LWC and N_w simultaneously increased around GWS of YDM when Lekima passed over the YDM: D_0 increased by about 0.5 mm from Fig. 13a to Fig. 13c in the enlarged area with $D_0>1.5$ mm; LWC increased more than three times to above 3 g$\cdot$m^{-3} from Fig. 13e to 13g; $\log_{10}(N_w)$ increased about 0.4~0.8 m$^{-3}\cdot$mm^{-1} from Fig. 13i to 13k. In addition, the gradual but insignificant increase of D_0, LWC and N_w persisted around GWS of KCM, including a diameter transition from $D_0<1.25$

400   mm to $D_0>1.5$ mm (Figs. 13a-13d); LWC increased by about 1g$\cdot$m^{-3} (Figs. 13e-13h) and $\log_{10}(N_w)$ increased about 0.4 m$^{-3}\cdot$mm^{-1}(Figs. 13i-13l). Although increased drop size still cannot make Z_{DR}^C close to $\hat{Z}_{DR}$, these simultaneous increases suggest the coexistence of coalescence and breakup following the serious collision process, and a potential chain reaction in which large-sized raindrops tend to break apart during the falling processes but broken droplets resulted in increased concentration of raindrops for higher collision efficiency.

405

The mountain terrain played an important role in boosting this process. The gradually increasing LWC from Fig. 13e to 13h around the GWS of YDM and KCM directly demonstrates this moisture-blocking effects caused by the mountain terrain. The topographical uplift of water vapors could further promote moisture convergence and aggravate the potential recirculation process of little droplets accompanying with the updrafts (Naumann and Seifert, 2016), which might be already serious due to

410   the vertical wind shear in typhoon. Enhanced collision efficiency is anticipated, which then contributes to the dynamic

coalescence-breakup balance prone to larger-sized and high concentrated raindrops. Resultantly, the abovementioned simultaneous increase of D_0, LWC and N_w coincide with the GWS areas of YDM and KCM.

As a result, more concentrated large-size raindrops could be anticipated near the surface than dwelling aloft. The main

415   consideration is that updraft cannot hold large-sized raindrops, and large-size raindrops fall faster than the smaller ones. This is also supported by the underestimated Z_{DR}^C distributed below the theoretical Z_{DR}-Z_H curve in Figs. 9c and 9d, as well as the evident larger $\hat{Z}_{DR}$ than Z_{DR}^C. In addition, some melted graupels transformed into big raindrops and then fell on the ground (indicated by the timeseries comparison in Sections 3.1.1 and 3.1.2). The complex microphysical process of this landfalling typhoon not only produce inconsistent Z_H-Z_{DR}-K_{DP} distribution in the storm, but also an inconsistency between radar

420   measurements and their surface counterparts. Such complex microphysical process should be considered in practical applications such as radar rainfall mapping.

3.3 Radar QPE Analysis

The quality-controlled DSD dataset through the processing procedure and analysis in Sections 2.3 and 3.1.1 is utilized, three basic radar rainfall rate relationships for $R(Z_H)$, $R(K_{DP})$, and $R(Z_H, Z_{DR})$ are respectively established as

425
$$R(Z_H) = 0.0544 \times Z_H^{0.608} \tag{11a}$$

$$R(K_{DP}) = 45.0484 \times K_{DP}^{0.7679} \tag{11b}$$

$$R(Z_H, Z_{DR}) = 0.0086 \times Z_H^{0.9153} Z_{DR}^{-3.8606} \tag{11c}$$

based on the standard weighted least squares nonlinear fitting method and DSD-derived radar variables (depicted in Fig. 14). In addition, Z_{DR}^M, Z_{DR}^C and $\hat{Z}_{DR}$ are respectively integrated with Z_H to exploit the impacts of the abovementioned microphysical

430   process on radar QPE algorithms. The pixel-to-pixel linear average accumulation scheme is utilized to retrieve radar six-hour rainfall fields for these radar QPE estimators and then evaluated independently by comparing gauge six-hour rainfall measurements through the absolute normalized mean error (E_{NMA}), root-mean-square error (E_{RMS}), and correlation coefficient (E_{CC}) as

$$E_{NMA} = \frac{\sum_{i=1}^{n} |r_i - g_i|}{\sum_{i=1}^{n} g_i} \times 100\% \tag{12a}$$

$$E_{RMS} = \sqrt{\frac{1}{n} \sum_{i=1}^{n} (r_i - g_i)^2} \tag{13b}$$

$$E_{CC} = \frac{\sum_{i=1}^{n} (r_i - \bar{r})(g_i - \bar{g})}{\sqrt{\sum_{i=1}^{n} (r_i - \bar{r})^2} \sqrt{\sum_{i=1}^{n} (g_i - \bar{g})^2}} \tag{13c}$$

where r_i and g_i respectively refers to radar rainfall estimates and gauge-measured rainfall. Six-hour radar rainfall fields

435   retrieved by $R(Z_H^M)$, $R(Z_H^C)$, $R(K_{DP})$, $R(Z_H^M, Z_{DR}^M)$, $R(Z_H^C, Z_{DR}^C)$, $R(Z_H^C, \hat{Z}_{DR})$ are respectively derived in Fig. 15, as well as the

scattergram between radar rainfall estimates and gauge rainfall measurements depicted in Fig. 16, to reveal their real performances around the disastrous area.

$R(Z_H^M)$ presents lower rainfall estimates in Fig. 15a than the other radar rainfall estimators in Figs. 15b-15f although they have
440   similar rainfall center shapes. In terms of statistical scores in Table 1, $R(Z_H^M)$ performs not worst among all radar rainfall estimators, its E_{RMS}, E_{NMA} and E_{CC} even outperform $R(Z_H^M, Z_{DR}^M)$ by 57%, 31.6% and 7.9%, and outperform $R(Z_H^C, Z_{DR}^C)$ by 63.8%, 34.9% and 6%, respectively. However, its underestimation can be easily perceived from the scatters in Fig. 16a, and $R(Z_H^M)$ mainly underestimates when rainfall recordings exceeds 100 mm in the center rainfall area. This phenomenon can be ascribed to the attenuation on Z_H^M caused the highly concentrated hydrometeors in the storm as abovementioned analysis, which
445   persists during the landfall of Lekima.

In contrast, $R(Z_H^C)$ in Fig. 15b presents higher rainfall estimates and $R(Z_H^C)$ mainly overestimates since more scatters are distributed above the diagonal line ($y = x$) as depicted in Fig. 16b, and its E_{CC} outperforms that of $R(Z_H^M)$ by 4.2% even with larger E_{RMS} and E_{NMA} scores. The overestimation of $R(Z_H^C)$ in the rainfall center area conversely demonstrates the effectiveness
450   of the attenuation correction based on the ZPHI method, because the same $R(Z_H)$ relationship is utilized for the rainfall retrieval, the only difference is the replacement of Z_H^M with Z_H^C.

$R(K_{DP})$ in Fig. 15c presents similar rainfall field structure with $R(Z_H^C)$. The scores of $R(K_{DP})$ are just a little superior to that of $R(Z_H^C)$ in Table 1 with its E_{RMS}, E_{NMA} and E_{CC} outperforming that of $R(Z_H^C)$ by 3.1%, 3.2% and 0.5%, respectively. And the
455   scattergrams in Figs. 16b and 16c are also similar to each other, indicating that $R(K_{DP})$ and $R(Z_H^C)$ both overestimates although $R(K_{DP})$ is less overestimated when rainfall recordings are less than 100mm. Their similar performances can be attributed to the consistency between radar-measured K_{DP} and Z_H^C measurements as described in Section 3.1.2.

$R(Z_H^M, Z_{DR}^M)$ and $R(Z_H^C, Z_{DR}^C)$ in Figs. 15d and 15e both present seriously higher estimates in the rainfall center area than the
460   others, which results in serious overestimation according to the scattergrams respectively in Figs. 16d and 16e. Furthermore, $R(Z_H^C, Z_{DR}^C)$ obtains the worst E_{RMS} and E_{NMA} scores of all radar rainfall estimators, and it can be explained based on the Z_H-related and Z_{DR}-related calculation items as demonstrated in Fig. 17: Z_H^C can make much higher rainfall estimates through Z_H-related item than Z_H^M, however, the calculation needs to be further adjusted through the Z_{DR}-related item: the larger Z_{DR} measurements correspond to less final rainfall estimates. A -0.5dB Z_{DR} bias could result in quite less rainfall adjustment
465   according to Fig. 17. The attenuation effects on Z_{DR}^M make corresponding rainfall calculation less adjusted, which can effectively account for the overestimation of $R(Z_H^M, Z_{DR}^M)$. however, the correction cannot make Z_{DR}^C completely consistent with Z_H^C but underestimated as demonstrated in Section 3.1.2, which is tightly related to the dynamic microphysical process

described in Section 3.2.

470   The spatial texture of $R(Z_H^C, \hat{Z}_{DR})$ in Fig. 15f presents slightly less rainfall estimates than $R(Z_H^C)$ and $R(K_{DP})$ in Figs. 15b and

15c, and the scattergram in Fig. 16f agrees better with gauge rainfall than that in Figs. 16b and 16c. $R(Z_H^C, \hat{Z}_{DR})$ is obviously

superior to $R(Z_H^M, Z_{DR}^M)$ and $R(Z_H^C, Z_{DR}^C)$ and the overestimation is largely reduced. The E_{RMS}/E_{NMA} score of $R(Z_H^C, \hat{Z}_{DR})$ performs

even better than $R(Z_H^C)$ and $R(K_{DP})$ respectively by 8.6/5% and 5.7/1.8%, although its E_{CC} score is slightly worse by 0.2% and

0.3%. The superiority of $R(Z_H^C, \hat{Z}_{DR})$ can be also apparently attributed to the incorporation of $\hat{Z}_{DR}$. Although $\hat{Z}_{DR}$ is not a real

475   radar measurement, it is directly estimated from Z_H^C from theoretical DSD-derived Z_{DR}-Z_H relationship in Eq. 2a. Therefore,

$\hat{Z}_{DR}$ is naturally self-consistent with Z_H^C and K_{DP}. The utilization of DSD-derived Z_{DR}-Z_H relationship intrinsically assumes that

raindrops composition in radar range gates have similar size and concentration to its surface counterparts, therefore, $\hat{Z}_{DR}$ is an

equivalent radar variable, no matter what the real raindrop size and concentration contribute to Z_H^C. The replacement of Z_{DR}^C

with $\hat{Z}_{DR}$ is also equivalent to imposing the surface raindrop size and concentration on radar measurements. As mentioned in

480   Section 3.2, $\hat{Z}_{DR}$ is relatively larger than Z_{DR}^C and larger adjustment can be performed for rainfall estimation using $R(Z_H^C, \hat{Z}_{DR})$

according to Fig. 17, which also indicates that larger raindrops were falling near the surface. In this way, better consistency

between radar measurements and surface measurements can also be achieved, which accounts for the superiority of $R(Z_H^C, \hat{Z}_{DR})$

to the other radar QPE estimators.

485   Unfortunately, there are no other disdrometers deployed within the rainfall center area, so it is hard to conduct a more complete

microphysical analysis around this area. The overall overestimation of $R(Z_H^C)$, $R(K_{DP})$ and $R(Z_H^C, \hat{Z}_{DR})$ can be attributed to the

potential situations: wind effects may make gauge rainfall less recorded (such as XJ, HJ and LH in 3.1.1); some little-sized

hydrometeors might deviate from their vertically falling location due to the advection caused by the strong tangential winds,

and it is evident for HSS. In both situations, even with enhanced self-consistency between radar measurements, radar QPE

490   algorithm may fail to achieve the best performance.

3.4. Discussion

The complex microphysical process of landing Lekima has been revealed based on the analysis about radar measurement self-

consistency and their consistency with gauge and disdrometer, and its impacts on the practical performances of radar QPE

algorithms have been also investigated. Several key issues on radar quantitative applications are still challenging in the future:

495   (i) High-quality DSD dataset could lay a solid foundation for polarimetric radar applications, such as the establishment

of the relationships between Z_H, Z_{DR}, K_{DP} and R. One-dimensional disdrometers (OTT or Thies) have been the main facilities

for the national meteorological stations in China to collect DSD measurements so far. If these eliminated diameter-velocity

measurements could be deeply refined and corrected into more adequate size class or velocity class, the quality of DSD-derived

polarimetric variables could also be further enhanced. Maybe deploying some two-dimensional disdrometers could bring about
more efficient utilization of these one-dimensional disdrometer measurements.

(ii) The self-consistent polarimetric radar measurements are important for some microphysical analysis and quantitative applications. The ZPHI method for attenuation correction on Z_H and Z_{DR} in this paper could be further extended with newly establishing Z_{DR}-Z_H relationships for X-band polarimetric radar. But there are still some other necessary quality issues to be solved: some serious ground clutters around radar sites may cause low ρ_{HV} and widespread negative Z_{DR} values; clear air echoes would cause serious fluctuations on Ψ_{DP}, which is frequent at radar sites with low altitudes; radar beam partial blockage on Z_H and Z_{DR} may degrade their quality in the affected range gates accordingly, etc. These issues usually need to be mitigated in advance before their further applications.

(iii) The spatial variety of precipitation types could be far more complex and single relationship between R and radar measurements may be not representative for all pixels within radar coverage. $R(Z_H)$, $R(K_{DP})$ and $R(Z_H, Z_{DR})$ relationships at each disdrometer station are different with each other as listed in Table 2, but statistically averaged relationships are utilized for rainfall retrieval in Section 3.3. Therefore, the residual differences between radar estimates and gauge measurements are still large even for $R(Z_H^C)$, $R(K_{DP})$ and $R(Z_H^C, \hat{Z}_{DR})$. Merging radar with gauge measurements may partly mitigate such differences to some extent, however, the large altitude gap between radar range gates and surface stations and the limited accuracy of gauge measurements (usually 0.1mm) may also hinder deriving potentially more optimal relationships.

(iv) The stratus cloud embedded in typhoon may cause more potential uncertainties for radar QPE algorithm. One issue is associated with the ML, in which larger Z_H measurements can be observed than that near the surface. This issue will be more serious if only higher elevations can be utilized due to the beam blockage of mountainous terrain. The Z_H measurements at high altitudes need to be corrected before the further retrieval of radar rainfall estimates. But this correction usually needs a prior-knowledge about the vertical microphysical precipitation variations. Different correction models need to be respectively developed for stratus, convective, and tropical storms.

(v) Hail and graupel contaminations on radar-measured K_{DP} are not obvious during typhoon Lekima. However, if these contaminated K_{DP} are utilized, $R(K_{DP})$ and $R(K_{DP}, Z_{DR})$ would both overestimate. Even through some identification algorithms can be used to differentiate hydrometeor types contained in radar range gates, some correction procedures are also necessary to mitigate the contaminations from mixed-phase hydrometeors.

Furthermore, deploying some cost-effective vertically pointing radar network around the complex mountainous terrain area, such as some X-band or Ka-band cloud radar and wind profilers, may effectively coordinate weather radar to explore some more vertical variations of precipitation. They can collaborate with each other to establish some more reasonable correction models based on the statistics of their vertical radar measurements.

4. Summary

530 This paper utilizes a host of data, including DSD, gauge rainfall measurements and WZ-SPOL radar observations, to analyze the complex microphysics of the storm accompanying with Lekima (2019). In addition, the potential impacts of precipitation microphysics on multi-source data consistency and radar QPE algorithms are demonstrated. The main findings are summarized as follows:

(i) DSD-derived rainfall and radar variables can be more consistent with gauge rainfall recordings and WZ-SPOL
535 radar observations after processing the wind effects, hail and graupel contaminations on diameter-velocity measurements.

(ii) The breakup overwhelms over coalescence as the main outcome of the collision process of raindrops, noticeably changes the self-consistency between radar measurements, which also accounts for phenomenon that high raindrop concentration other than large size contributes more to large Z_H of the storm and the residual large deviation of Z_{DR}^C from $\hat{Z}_{DR}$ even after the attenuation correction.

540 (iii) $R(Z_H^C)$ performs comparably well with $R(K_{DP})$ owning to attenuation correction. But direct incorporation of Z_{DR} conversely make $R(Z_H, Z_{DR})$ perform worse with serious overestimation, which is also caused by the special microphysical process in typhoon.

(iv) $R(Z_H^C, \hat{Z}_{DR})$ outperforms $R(Z_H^C)$ and $R(K_{DP})$ in terms of the E_{RMS} and E_{NMA} scores, and it benefits from the better self-consistency between Z_H^C, $\hat{Z}_{DR}$ and K_{DP} and their consistency with surface counterparts. This is featured with less
545 sensitiveness to the real hydrometeor size and concentration in the storm.

The complex precipitation microphysics may have some unknown negative impacts on the consistency between multi-source datasets, which is still a challenge for the quantitative applications of polarimetric radar measurements. In-depth understanding of such microphysical processes is critical for the improvements. Combining scanning radar with vertically pointing radar, as
550 well as surface disdrometer and gauge measurements, is promising to reveal and model the vertical variations of precipitation with mixed-phase hydrometeors. Then correction schemes could be designed based on the new models to mitigate negative impacts related to the precipitation microphysical processes.

Author contributions

Yabin Gou carried out the data collection and detailed analysis. He was also part of the polarimetric radar data processing and
555 product generation team. Haonan Chen supervised the work and provided critical comments. Yabin Gou and Haonan Chen wrote the manuscript. Lulin Xue reviewed and edited the manuscript.

Declaration of Competing Interest

The authors declare that they have no known competing financial interests or personal relationships that could have appeared to influence the work reported in this paper.

560 **Acknowledgements**

This research is primarily supported by the National Natural Science Foundation of China under Grants 41375038. The work of H. Chen is supported by Colorado State University and the National Oceanic and Atmospheric Administration through (NOAA) through Cooperative Agreement NA19OAR4320073. The authors acknowledge the anonymous reviewers for their careful review and comments on this article. The S-band polarimetric radar, disdrometer and rain gauge data are provided by
565 the Chinese Meteorological Administration and are available upon request. Photos in Fig. 2(a) and (c) were retrieved from zj.weather.com.cn, in Fig. 2(b), (d) and (e) were obtained from sohu.com, and the one in Fig. 2(f) was obtained from www.chinanews.com.cn.

References

Bao, X., Wu, L., Zhang, S., Yuan, H., and Wang, H. 2020. A comparison of convective raindrop size distributions in the
570 eyewall and spiral rainbands of Typhoon Lekima (2019). Geophysical Research Letters, 47, e2020GL090729, doi:10.1029/2020GL090729

Beard, K. V., 1977. Terminal velocity adjustment for cloud and precipitation drops aloft. J. Atmos. Sci., 34, 1293–1298.

Brandes, E.A., Zhang, G., Vivekanandan, J. 2002. Experiments in rainfall estimation with a polarimetric radar in a subtropical environment. J. Appl. Meteorol., 41, 674–685.

575 Bringi, V.N.; Keenan, T.D.; Chandrasekar, V. Correcting C-band Radar Reflectivity and Differential Reflectivity Data for Rain Attenuation: A Self-consistent Method with Constraints. IEEE Trans. Geosci. Remote Sens. 2001, 39, 1906–1915.

Bringi, V.N.; Rico-Ramirez, M.A.; Thurai, M. 2010. Rainfall Estimation with An Operational Polarimetric C-Band Radar in the United Kingdom: Comparison with A Gauge Network and Error Analysis. J. Hydrometeorol., 12, 935–954.

Carlin, J.T.; Gao, J.; Snyder, J.C.; Ryzhkov, A.V. 2017. Assimilation of ZDR Columns for Improving the Spinup and Forecast
580 of Convective Storms in Storm-Scale Models: Proof-of-Concept Experiments. Mon. Weather Rev., 145, 5033–5057.

Chandrasekar, V.; Chen, H.; Philips, B. 2018. Principles of high-resolution radar network for hazard mitigation and disaster management in an urban environment. J. Meteor. Soc. Japan., 96A,119–139.

Chen, H., R. Cifelli and A. White, 2020: Improving Operational Radar Rainfall Estimates Using Profiler Observations Over Complex Terrain in Northern California. IEEE Transactions on Geoscience and Remote Sensing, 58(3), 1821-1832.

585 Cifelli, R.; Chandrasekar, V.; Chen, H.; Johnson, L.E. High Resolution Radar Quantitative Precipitation Estimation in the San Francisco Bay Area: Rainfall Monitoring for the Urban Environment. J. Meteorol. Soc. Jpn. 2018, 96A, 141–155.

Chen, H.; Chandrasekar, V.; Bechini, R. 2017.An Improved Dual-Polarization Radar Rainfall Algorithm (DROPS2.0):

Application in NASA IFloodS Field Campaign. J. Hydrometeor., 18, 917–937.

Donavon RA and Jungbluth KA. 2007. Evaluation of a technique for radar identification of large hail across the upper midwest
590 and central plains of the United States. Weather Forecast 22:244–254.

Frasier, S; Kabeche, F.; Ventura, J. F. I.; Al-Sakka, H.; Bousquet, O.. 2013. In-situ estimation of wet-radome attenuation at x-band. J Atmos Ocean Technol., 30(5), 917.

Friedrich, K., Higgins, S. A., Masters, F. J., and Lopez, C. R. 2013. Articulating and stationary PARSIVEL disdrometer measurements in conditions with strong winds and heavy rainfall. J Atmos Ocean Technol., 30(9), 2063–2080,
595 doi:10.1175/JTECH-D-12-00254.1

Gosset, M., E. P. Zahirib, and S. Moumounic. 2010. Rain Drop Size Distribution Variability and Impact on X-band Polarimetric Radar Retrieval: Results from the AMMA Campaign in Benin. Quart. J. Roy. Meteor. Soc., 136, 243–256.

Gou, Y., H. Chen and V. Chandrasekar, 2020. A Dynamic Approach to Quantitative Precipitation Estimation Using Multiradar Multigauge Network. IEEE Trans Geosci Remote Sens., 58(9),6376-6390, doi: 10.1109/TGRS.2020.2976724.

600 Gou Y, Chen H, Zheng J. 2019. Polarimetric Radar Signatures and Performance of Various Radar Rainfall Estimators during an Extreme Precipitation Event over the Thousand-Island Lake Area in Eastern China. Remote Sensing.,11(20):2335. https://doi.org/10.3390/rs11202335.

Gou, Y., Ma, Y., Chen, H. and Wen, Y.2018. Radar-derived Quantitative Precipitation Estimation in Complex Terrain over The Eastern Tibetan Plateau. Atmos. Res., 203, 286–297.

605 Hubbert, J.; Bringi, V.N. 1995. An Iterative Filtering Technique for The Analysis of Copolar Differential Phase and Dual Frequency Radar Measurements. J. Atmos. Ocean. Technol., 12, 643–648.

Hubbert, J.; Dixon, M.; Ellis, S. Weather Radar Ground Clutter. 2009. Part II: Real-Time Identification and Filtering. J. Atmos. Ocean. Technol., 26, 1181–1197.

Keenan, T. D., L. D. Carey, D. S. Zrnic', and P. T. May. 2001. Sensitivity of 5-cm Wavelength Polarimetric Radar Variables
610 to Raindrop Axial Ratio and Drop Size Distribution. J. Appl. Meteor., 40, 526–545.

Lee G, Zawadzki I .2005. Variability of drop size distributions: time-scale dependence of the variability and its effects on rain estimation. J Appl Meteorol 44:241–255.

Matrosov, S. Y. 2010. Evaluating polarimetric X-band radar rainfall estimators during HMT. J. Atmos. Oceanic Technol., 27, 122–134.

615 Mishra, K. V., Krajewski, W. F., Goska, R., Ceynar, D., Seo, B., Kruger, A., Niemeier, J. J., Galvez, M. B., Thurai, M., Bringi, V. N., Tolstoy, L., Kucera, P. A., Petersen, W. A., Grazioli, J., and Pazmany, A. L. 2016. Deployment and Performance Analyses of High-resolution Iowa XPOL Radar System during the NASA IFloodS Campaign. J. Hydrometeor., 17, 455–479.

Naumann, A. K., & Seifert, A. (2016). Recirculation and growth of raindrops in simulated shallow cumulus. Journal of Advances in Modeling Earth Systems, *8*(2), 520–537.

620 Park, S., M. Maki, K. Iwanami, V.N. Bringi, and V. Chandrasekar. 2005. Correction of Radar Reflectivity and Differential

Reflectivity for Rain Attenuation at X Band. Part II: Evaluation and Application. J. Atmos. Oceanic Technol., 22, 1633–1655.

Ryzhkov, A.V.; Giangrande, S.E.; Schuur, T.J. 2005.Rainfall Estimation with A Polarimetric Prototype of WSR-88D. J. Appl. Meteorol., 44, 502–515.

Ryzhkov, A.V.; Diederich, M.; Zhang, P.; Simmer, C. 2014. Potential Utilization of Specific Attenuation for Rainfall
625   Estimation, Mitigation of Partial Beam Blockage, and Radar Networking. J. Atmos. Ocean. Technol., 31, 599–619.

Schneebeli, M., and A. Berne. 2012.An extended Kalman Filter Framework for Polarimetric X-band Weather: Radar Data Processing. J. Atmos. Oceanic Technol., 29, 711–730.

Snyder, J.C.; Ryzhkov, A.V.; Kumjian, M.R.; Khain, A.P.; Picca, J. 2015. A ZDR Column Detection Algorithm to Examine Convective Storm Updrafts. Weather Forecast., 30, 1819–1844.

630   Tokay, A. and Bashor, P. G. 2010. An experimental study of small-scale variability of raindrop size distribution. Journal of Applied Meteorology and Climatology, 49(11), 2348–2365, doi:10.1175/2010JAMC2269.1

Tokay A, Bashor PG, Wolff KR.2005. Error characteristics of rainfall measurements by collocated Joss-Waldvogel disdrometers. J Atmos Ocean Technol 22:513–527.

Wang, Y.; Chandrasekar, V. 2009. Algorithm for Estimation of The Specific Differential Phase, J. Atmos. Ocean. Technol.,
635   26, 2565–2578.

Wang, Y., S. Cocks, L. Tang, A. Ryzhkov, P. Zhang, J. Zhang, and K. Howard.2019. A prototype quantitative precipitation estimation algorithm for operational S-Band polarimetric radar utilizing specific attenuation and specific differential phase. Part I: Algorithm description. J. Hydrometeor., 20, 985–997.

Zhang, J., Howard, K., Langston, C., Vasiloff, S., Kaney, B., Arthur, A., Van Cooten, S., Kelleher, K., Kitzmiller, D., Ding,
640   F., Seo, D., Wells, E., and Dempsey, C., 2011. National Mosaic and Multi-Sensor QPE (NMQ) system: Description, results, and future plans. Bull. Amer. Meteor. Soc., 92, 1321–1338, doi:10.1175/2011BAMS-D-11-00047.1.

Table 1. Evaluation scores of six-hour rainfall accumulations based on six radar QPE relations.

Scores	Radar QPE Relations					
	$R(Z_H^M)$	$R(Z_H^C)$	$R(K_{DP})$	$R(Z_H^M, Z_{DR}^M)$	$R(Z_H^C, Z_{DR}^C)$	$R(Z_H^C, \hat{Z}_{DR})$
E_{RMS}(mm)	35.2066	50.0166	48.4374	82.269	97.2031	45.6924
E_{NMA}	29.0485	31.9173	30.8652	42.499	44.6513	30.3174
E_{CC}	0.7634	0.7954	0.7995	0.7075	0.7201	0.7971

645

Table 2. Radar QPE relations obtained at six different meteorological stations.

Stations	Radar QPE Relations		
	$R(Z_H)$	$R(K_{DP})$	$R(Z_H, Z_{DR})$
XJ	$0.0502 \times Z_H^{0.6332}$	$50.3159 \times K_{DP}^{0.7755}$	$0.0077 \times Z_H^{0.9308} Z_{DR}^{-4.0151}$
LH	$0.0397 \times Z_H^{0.6678}$	$53.0847 \times K_{DP}^{0.7775}$	$0.0093 \times Z_H^{0.909} Z_{DR}^{-3.9326}$
HJ	$0.0202 \times Z_H^{0.7398}$	$58.0381 \times K_{DP}^{0.8320}$	$0.0077 \times Z_H^{0.9390} Z_{DR}^{-4.2782}$
DT	$0.0332 \times Z_H^{0.6775}$	$41.8480 \times K_{DP}^{0.8314}$	$0.0062 \times Z_H^{0.9526} Z_{DR}^{-4.1799}$
YH	$0.0174 \times Z_H^{0.7131}$	$45.1785 \times K_{DP}^{0.8264}$	$0.0084 \times Z_H^{0.9086} Z_{DR}^{-3.5505}$
WL	$0.0203 \times Z_H^{0.6891}$	$54.1236 \times K_{DP}^{0.8177}$	$0.0072 \times Z_H^{0.9426} Z_{DR}^{-4.0677}$
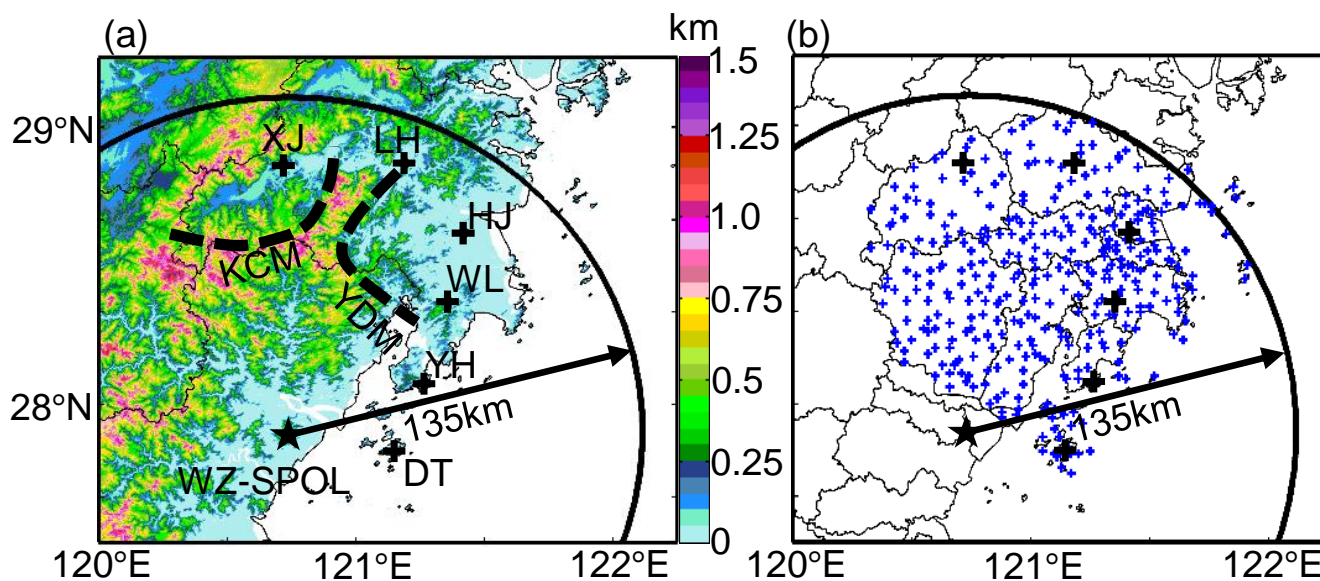
Fig. 1. (a) Terrain elevation and disdrometer network around the WZ-SPOL radar; (b) rain gauge network around the disaster center area. The black star in (a) and (b) denotes the location of the WZ-SPOL radar. The black "+" in (a) and (b) refer to the locations of six national meteorological stations, where Thies disdrometers are deployed. The blue "+" in (b) refers to regional meteorological stations where rain gauges are deployed.

Fig. 2. The disastrous situation in WZ and TZ due to the landfall of super typhoon Lekima: (a) high waves along Wen Ling (WL) coast of TZ city; (b) landslide in the north mountain area of Yong Jia (YJ) in WZ city; (c)-(f) indicate the serious waterlogging in WL, Lin Hai (LH), Yu Huan (YH), and Xian Ju (XJ) town of TZ city.
Photo (a) is available at http://picture.youth.cn/qtdb/201908/t20190810_12036586.htm.
Photo (b) is available at https://baijiahao.baidu.com/s?id=1641647981934061656&wfr=spider&for=pc.
Photo (c) is available at https://new.qq.com/omn/20190810/20190810A0FZUT00.html?pc.
Photo (d) is available at https://new.qq.com/omn/20190828/20190828A0KGLT00.html.
Photo (e) is available at https://www.newssz.com/sz/2019/0818/94241-1/.
Photo (f) is available at https://m.chinanews.com/wap/detail/undefined/zw/8925613.shtml.
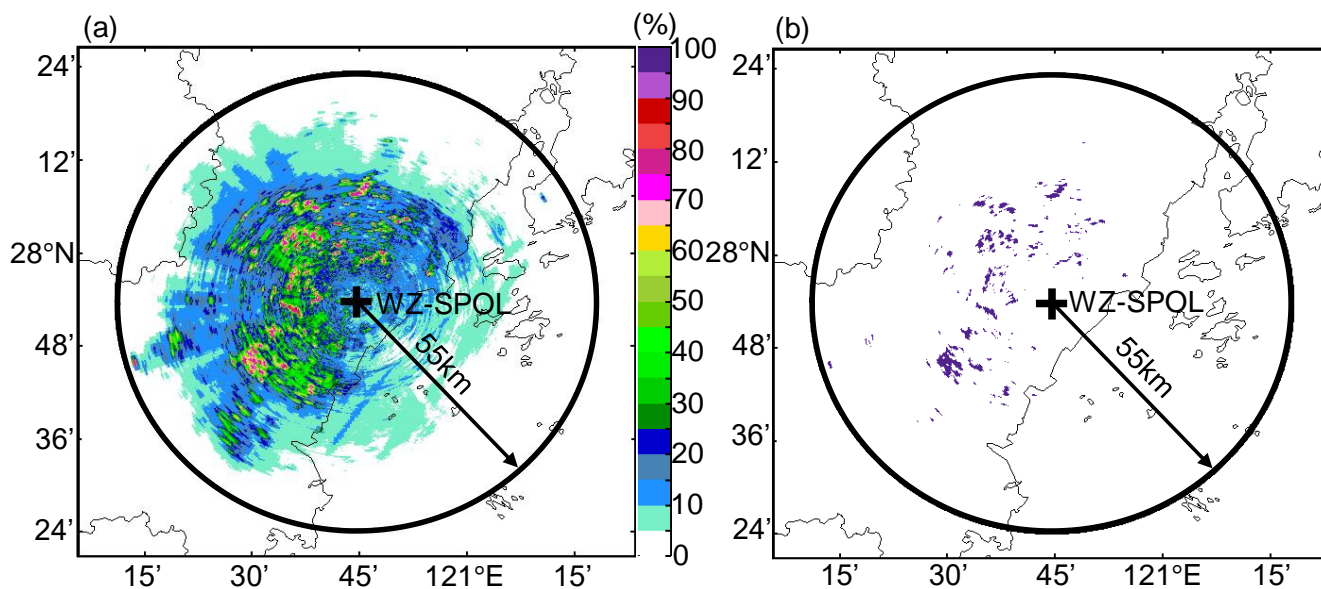
Fig. 3. (a) Statistics of pixels with $Z_H > 0$ dBZ within 55 km from the WZ-SPOL radar; (b) Residual static ground clutter mask of the WZ-SPOL radar.
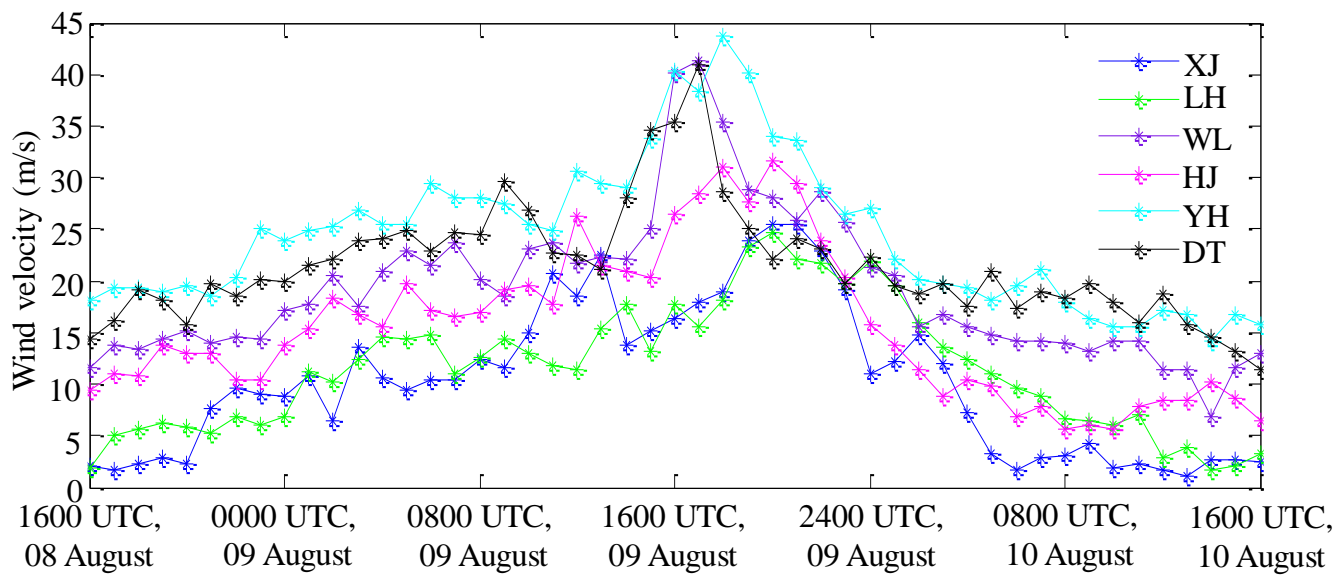
Fig. 4. Time series of hourly maximum wind speed at the six national meteorolgoical stations during 1600 UTC, 08 August 2019 and 1600 UTC, 10 August 2019.

680
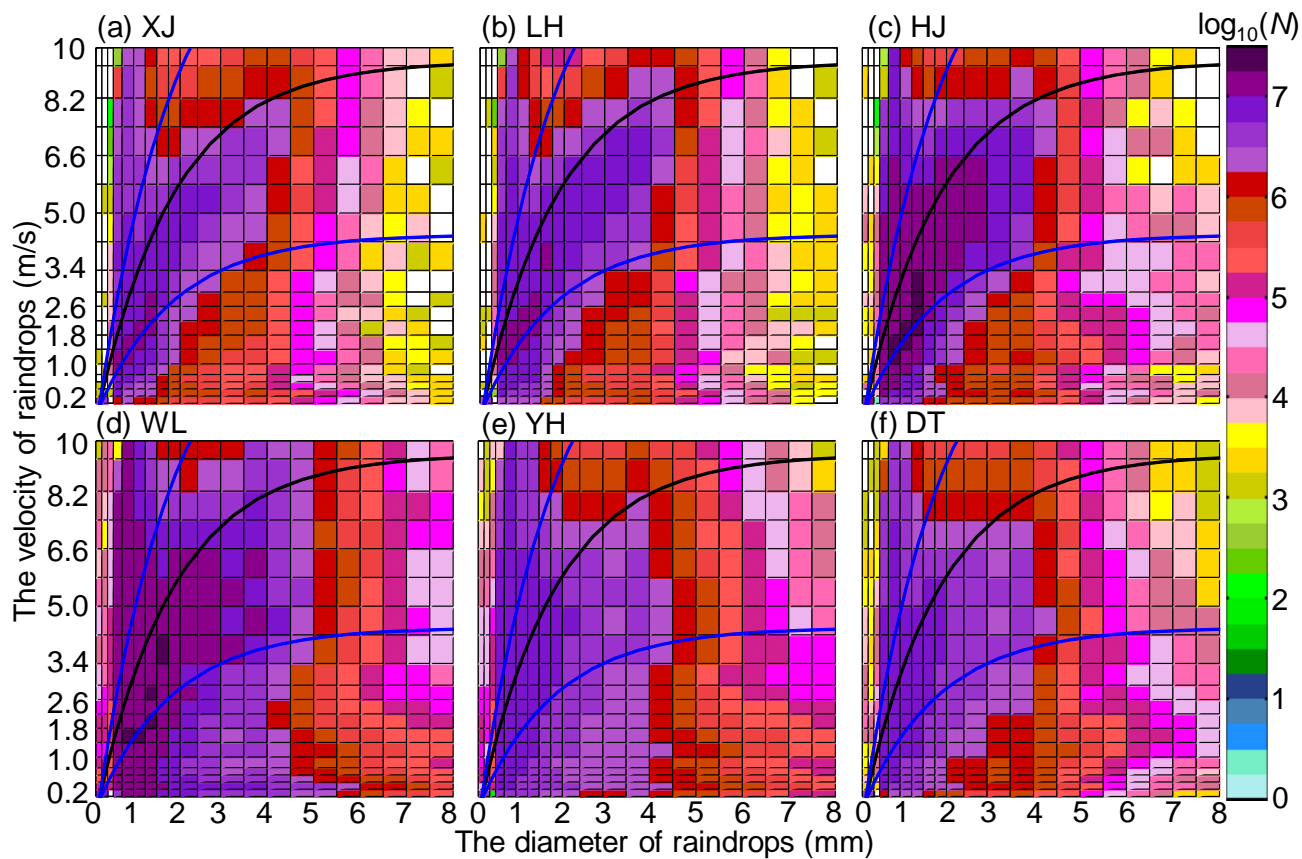
Fig. 5. The original velocity–diameter dataset collected at (a) XJ, (b) LH, (c) HJ, (d) WL, (e) YH, and (f) DT. The black line and two blue lines refer to the fall speed V_B, $0.5V_B$ and $1.5V_B$ calculated in Eq. 3, respectively.
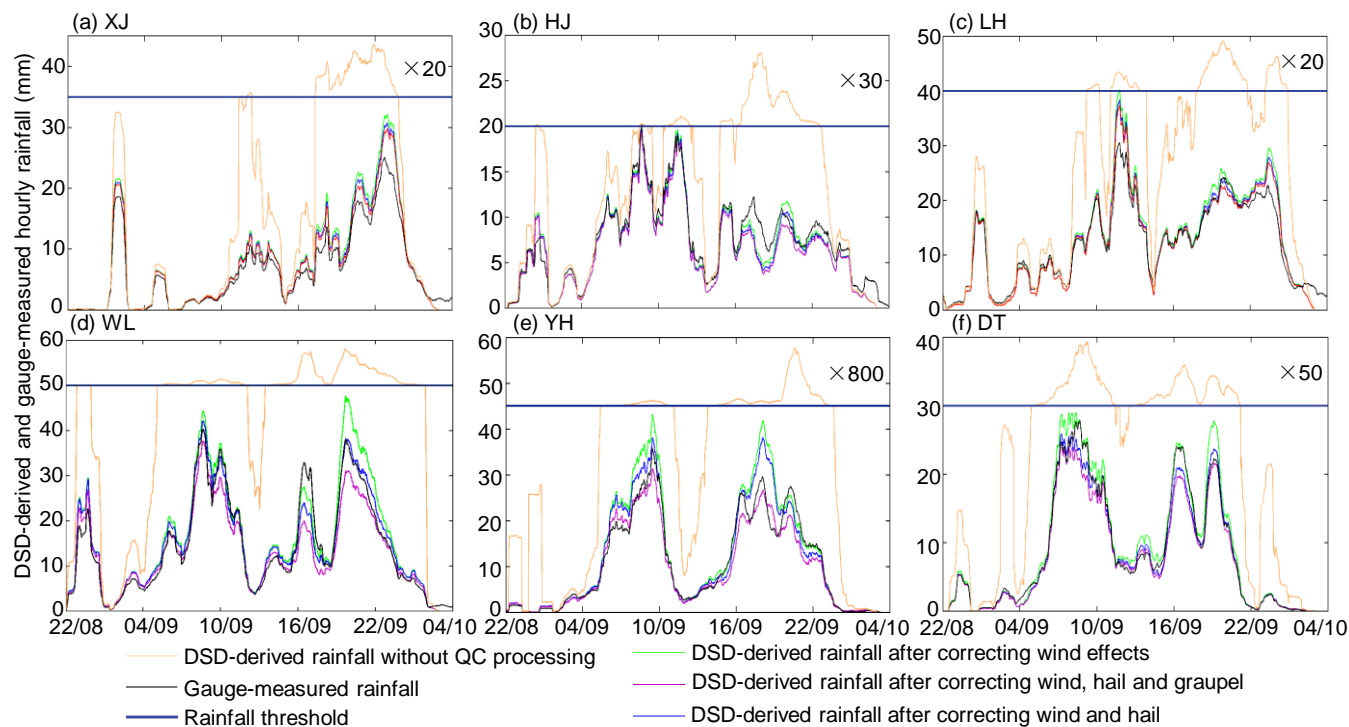
Fig. 6. Time series of DSD-derived and gauge-measured hourly rainfall: (a)-(f) are obtained from XJ, HJ, LH, WL, YH and DT, respectively, during 2200 UTC 08 August 2019 and 0400 UTC 10 August 2019. The number behind "×" refers to CT and bold dark
690 **blue lines indicate the threshold of RT of each station according to Eq. (5).**
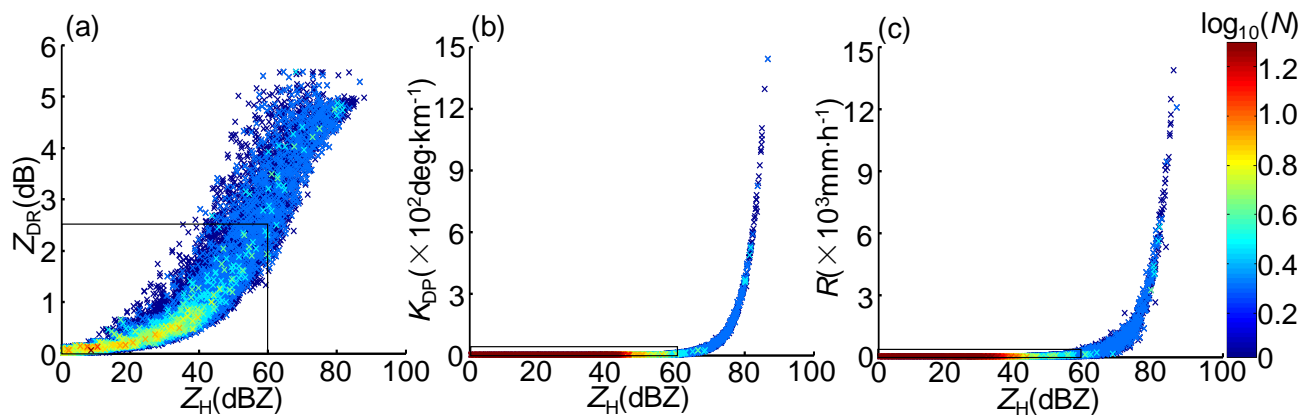
695   **Fig. 7. The scattergrams of DSD-derived polarimetric radar variables without QC on the DSD data: (a) Z_{DR} vs. Z_H; (b) K_{DP} vs. Z_H; (c) R vs. Z_H. The rectangles in (a)-(c) indicate the ranges of DSD-derived variables after final QC processing.**
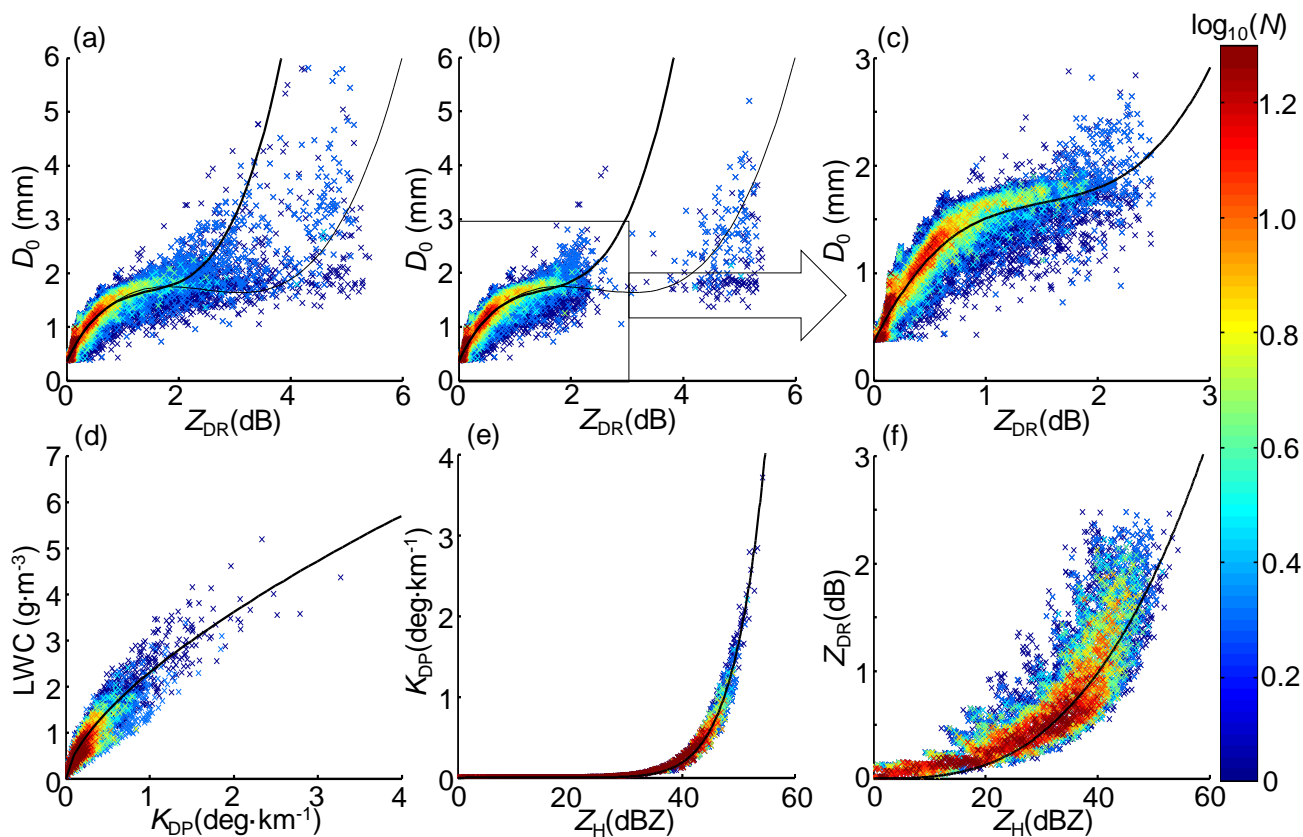
**Fig. 8. Scattergrams between polarimetric radar variables: (a) D_0 vs. Z_{DR} after eliminating wind contaminations. (b) is based on (a),
but after further removing the hail and graupel contaminations. (c) is based on (b), but after further eliminating the residual graupel
contaminations with $Z_{DR}>2.5dB$. (d), (e) and (f) are LWC vs. K_{DP}, K_{DP} vs. Z_H, Z_{DR} vs. Z_H based on the same dataset with (c). The thick
black lines in (a)-(c) stand for Eq. 5; the thin black lines in (a) and (b) indicate the overfitted results, and the black curves in (d)-(f)
stand for Eq. 6, Eq. 7 and Eq. 2a, respectively.**
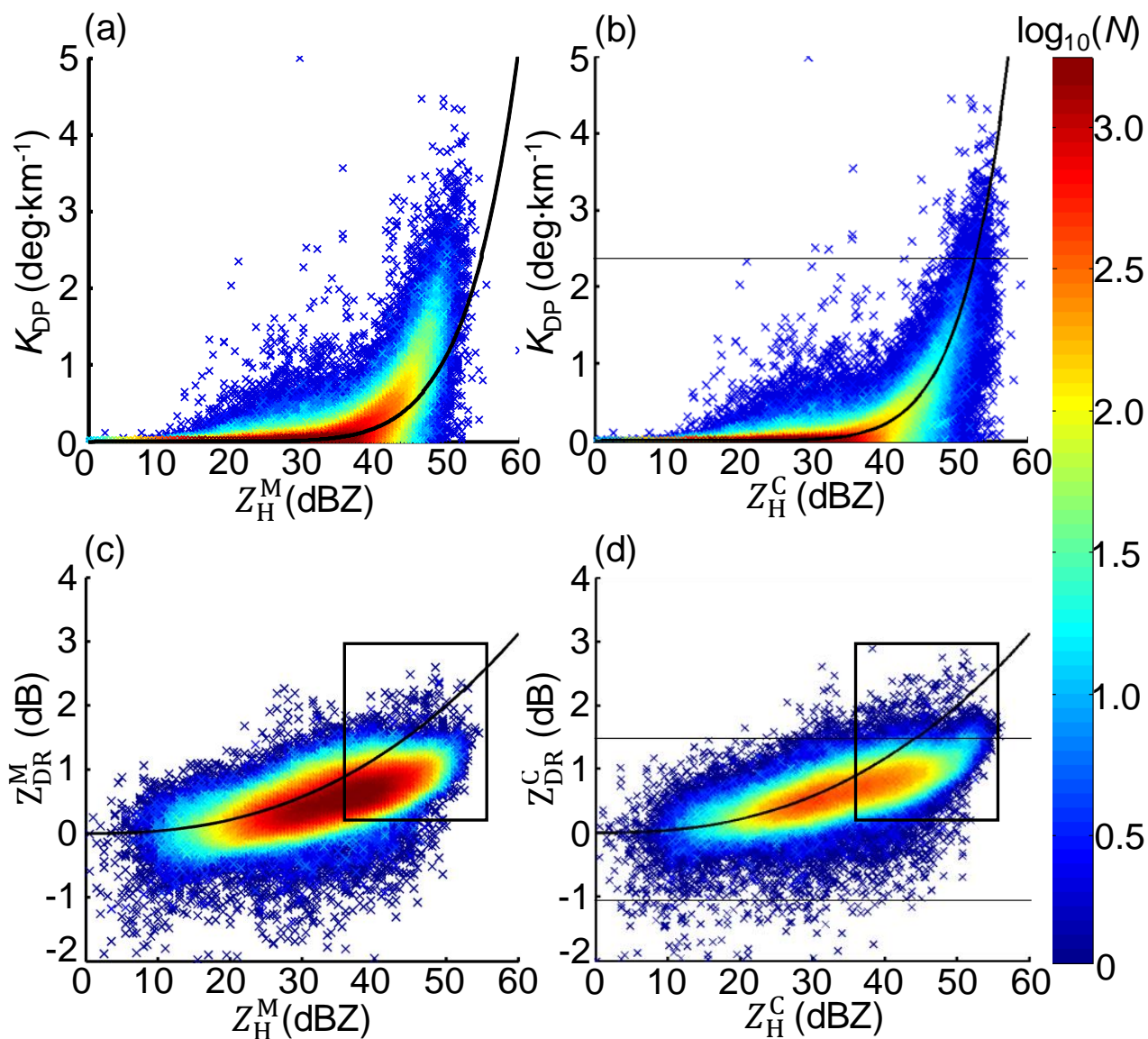
Fig. 9. The scattergram between polarimetric measurements from WZ SPOL: (a) K_{DP} vs Z_H^M; (b) K_{DP} vs Z_H^C; (c) Z_{DR}^M vs Z_H^M; (d) Z_{DR}^C vs Z_H^C.
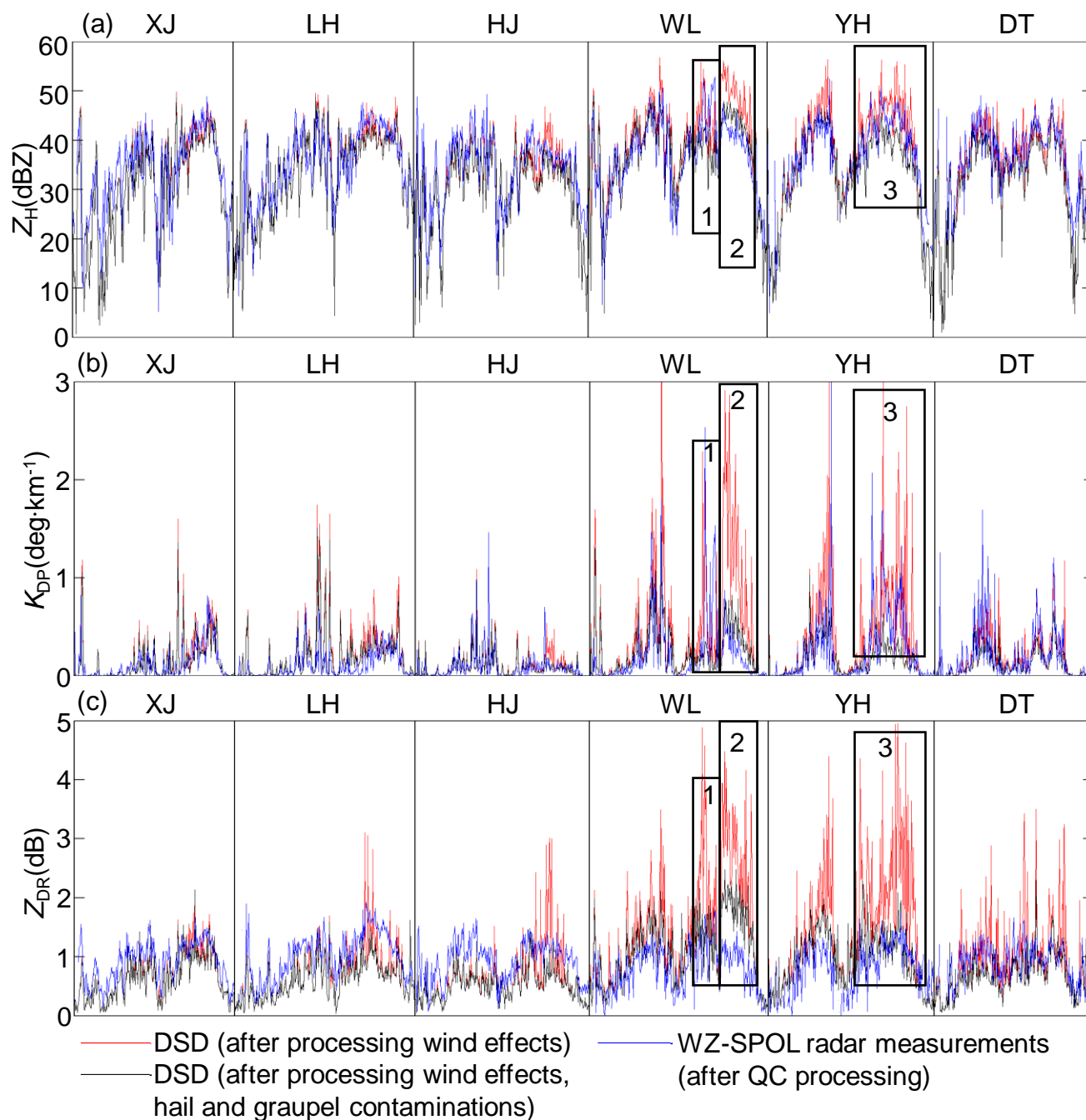
Fig. 10. (a) Time series of radar-measured Z_H^C and DSD-derived Z_H at the six meteorological stations shown in Fig. 6 during 2200 UTC 08 August 2019 and 0400 UTC 10 August 2019; (b) Similar to (a), but for radar-measured K_{DP} and DSD-derived K_{DP}; (c) Similar to (a), but for radar-measured Z_{DR}^C and DSD-derived Z_{DR}.
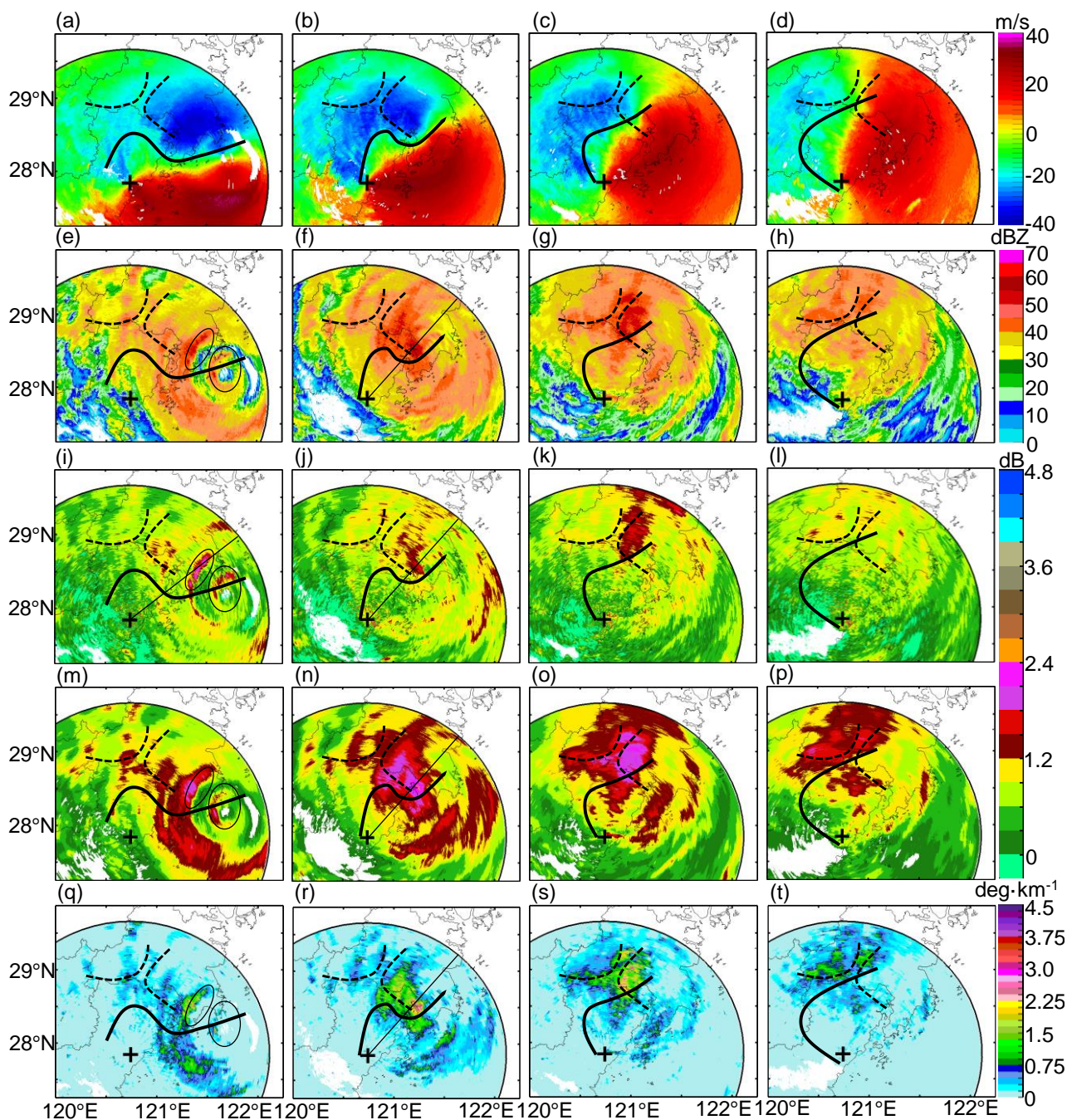
Fig. 11. WZ-SPOL radar measurements during typhoon Lekima: (a)-(d) are Doppler velocity V_R at 1601 UTC, 1759 UTC, 2002 UTC, and 2200 UTC, 09 August 2019, respectively; (e)-(h), (i)-(l), (m)-(p), (q)-(t) are Z_H^C, Z_{DR}^C, $\widehat{Z}_{DR}$, and K_{DP} at the same time as (a)-(d). The black solid lines refer to wind shear deduced from V_R. The black dashed lines refer to the GWS of KCM and YDM, and "+" indicates the location of WZ-SPOL radar. The ellipses in (e), (i), (m) and (q) indicate where hydrometeor size sorting occurred. The black lines along the radial profiles in (f), (j), (n) and (r) indicate the azimuthal angle shown in Fig. 12.
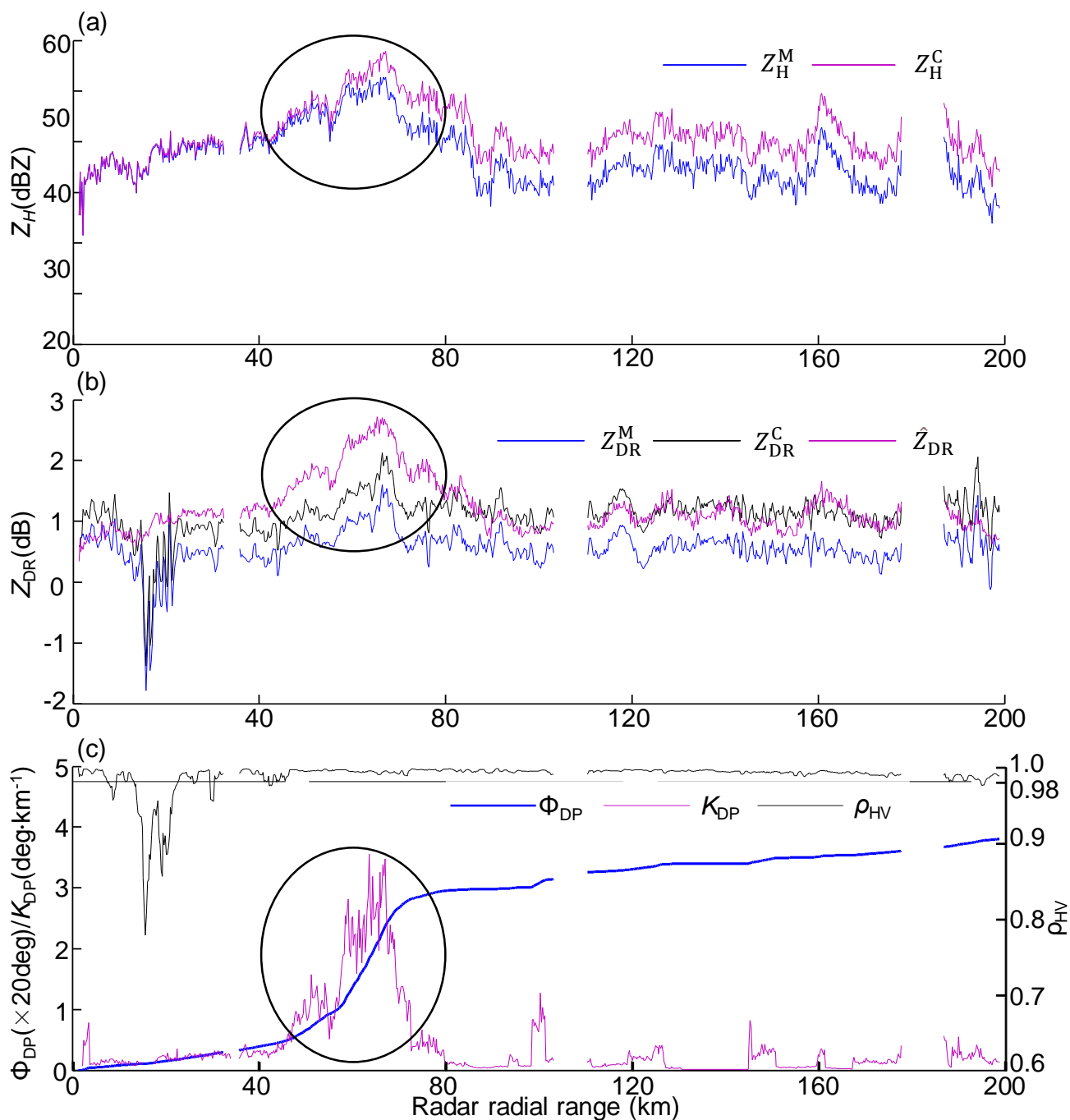
Fig. 12. (a) Z_H^C vs. Z_H^M, (b) Z_{DR}^M and Z_{DR}^C, (c) Φ_{DP}, K_{DP} and ρ_{HV} measurements along a radial profile of WZ-SPOL radar (azimuth angle = 46°) at elevation angle of 0.5° at 1759 UTC, 09 August 2019. This azimuth angle is highlighted in Fig. 11.
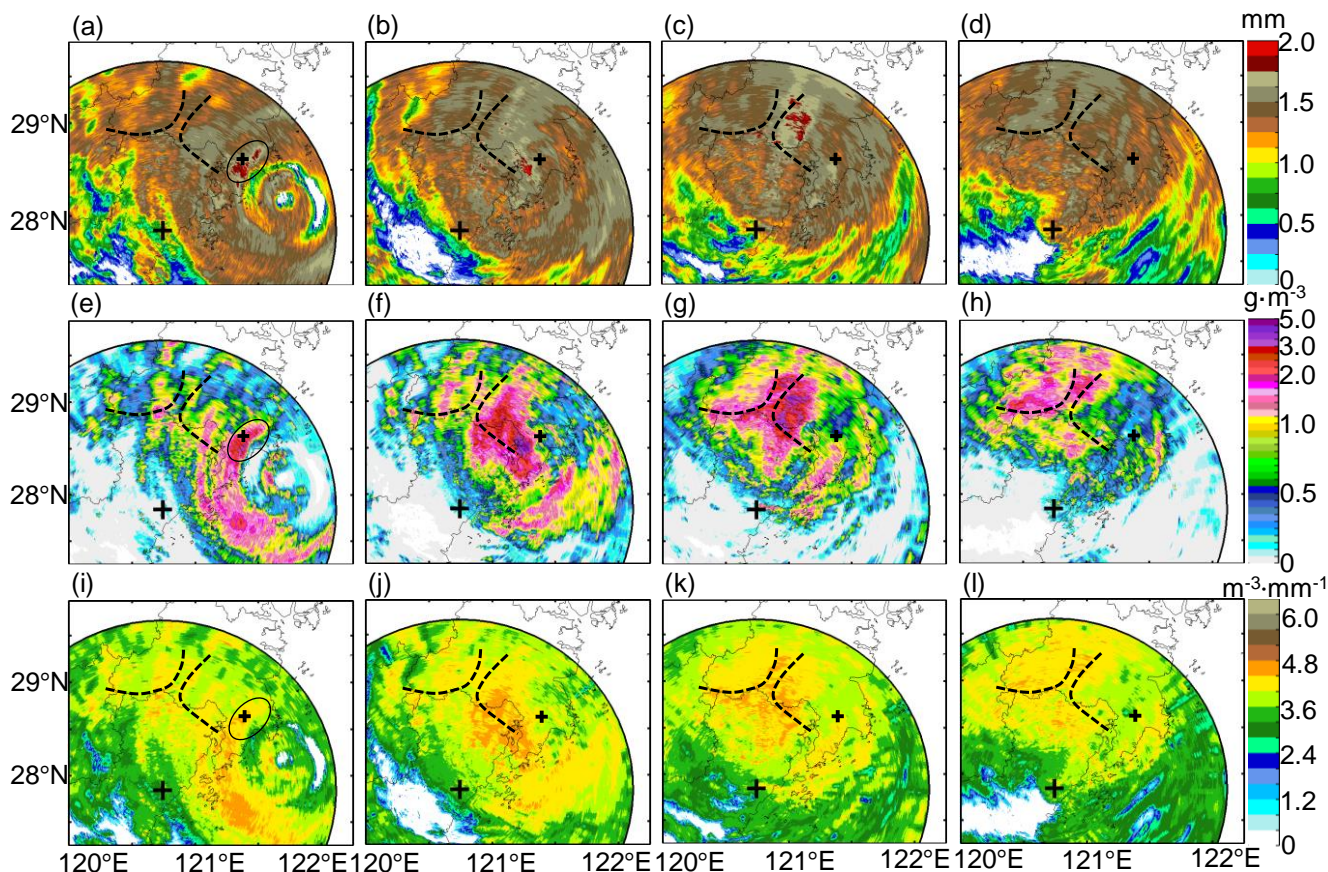
720 **Fig. 13. Radar-retrieved DSD parameters during typhoon Lekima: (a)-(d) are D_0 at 1601 UTC, 1759 UTC, 2002 UTC, and 2200 UTC, 09 August 2019, respectively; (e)-(h) and (i)-(l) (t) are LWC and $\log_{10}(N_w)$ at the same time as (a)-(d). The large "+" indicates the location of WZ-SPOL radar and little "+" indicates the location of WL station. The black dashed lines refer to the GWS of KCM and YDM.**

725
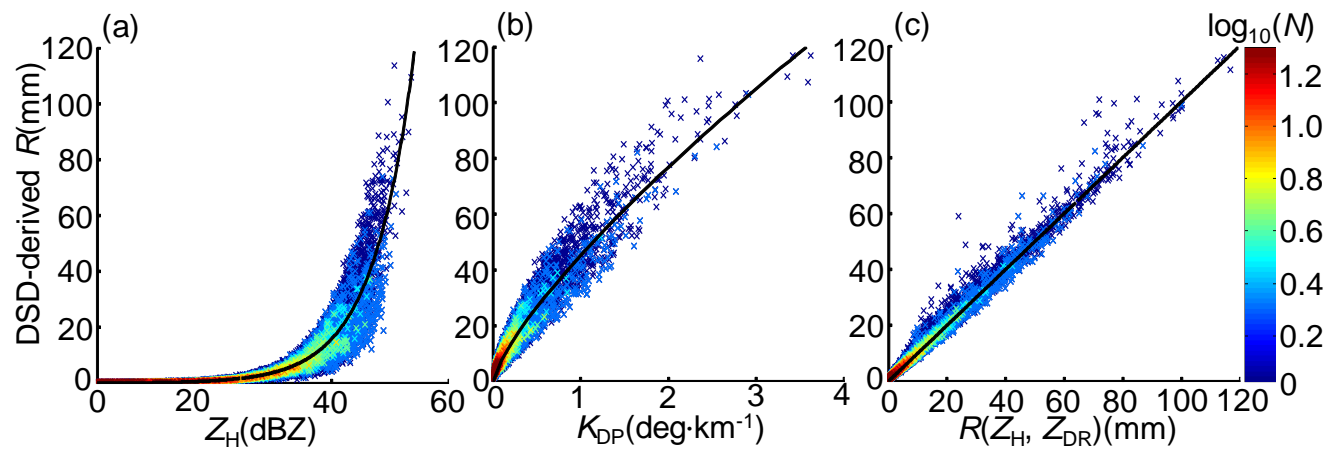
Fig. 14. The scattergram of (a) DSD-derived R vs. Z_H, (b) DSD-derived R vs. K_{DP}, (c) DSD-derived R vs. R estimated by fitted $R(Z_H, Z_{DR})$.
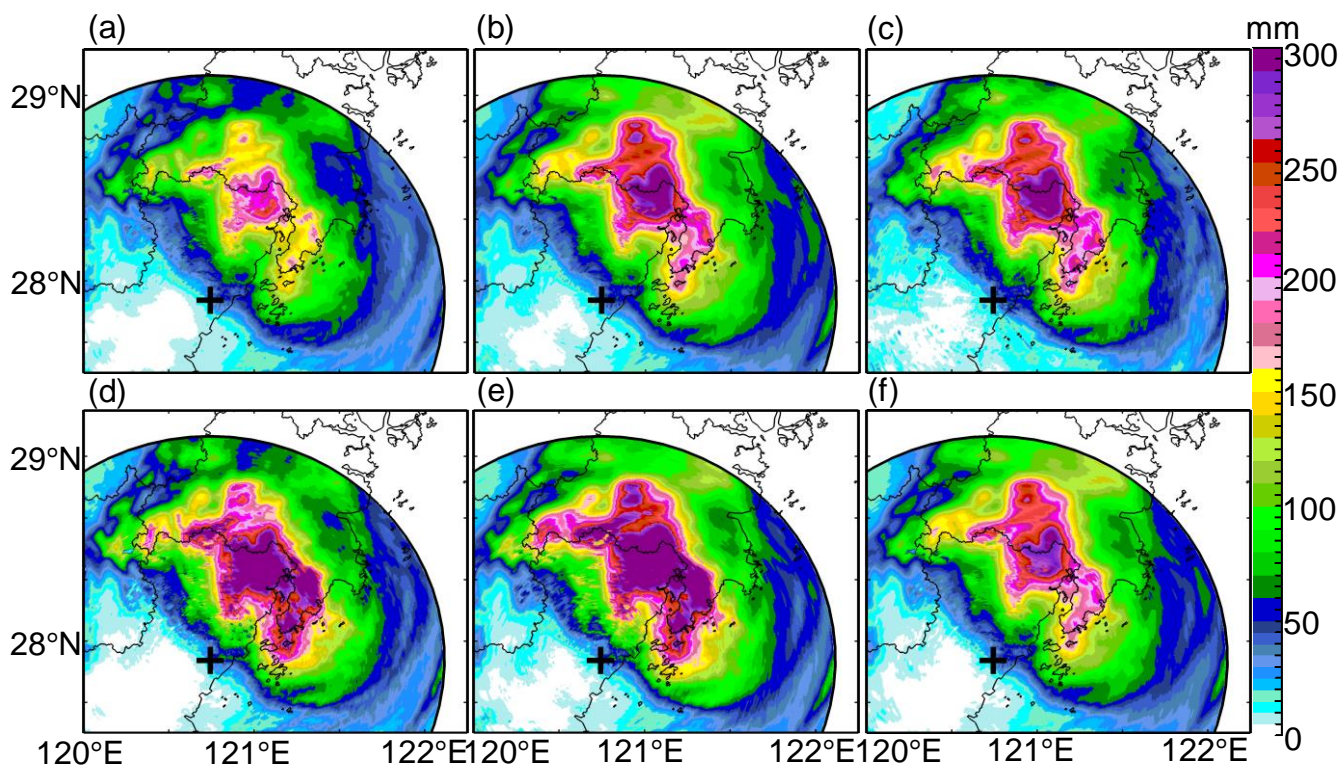
Fig. 15. Six-hour rainfall estimates derived from (a) $R(Z_H^M)$, (b) $R(Z_H^C)$, (c) $R(K_{DP})$, (d) $R(Z_H^M, Z_{DR}^M)$, (e) $R(Z_H^C, Z_{DR}^C)$, and (f) $R(Z_H^C, \widehat{Z}_{DR})$ at 2200 UTC 09 August 2019.
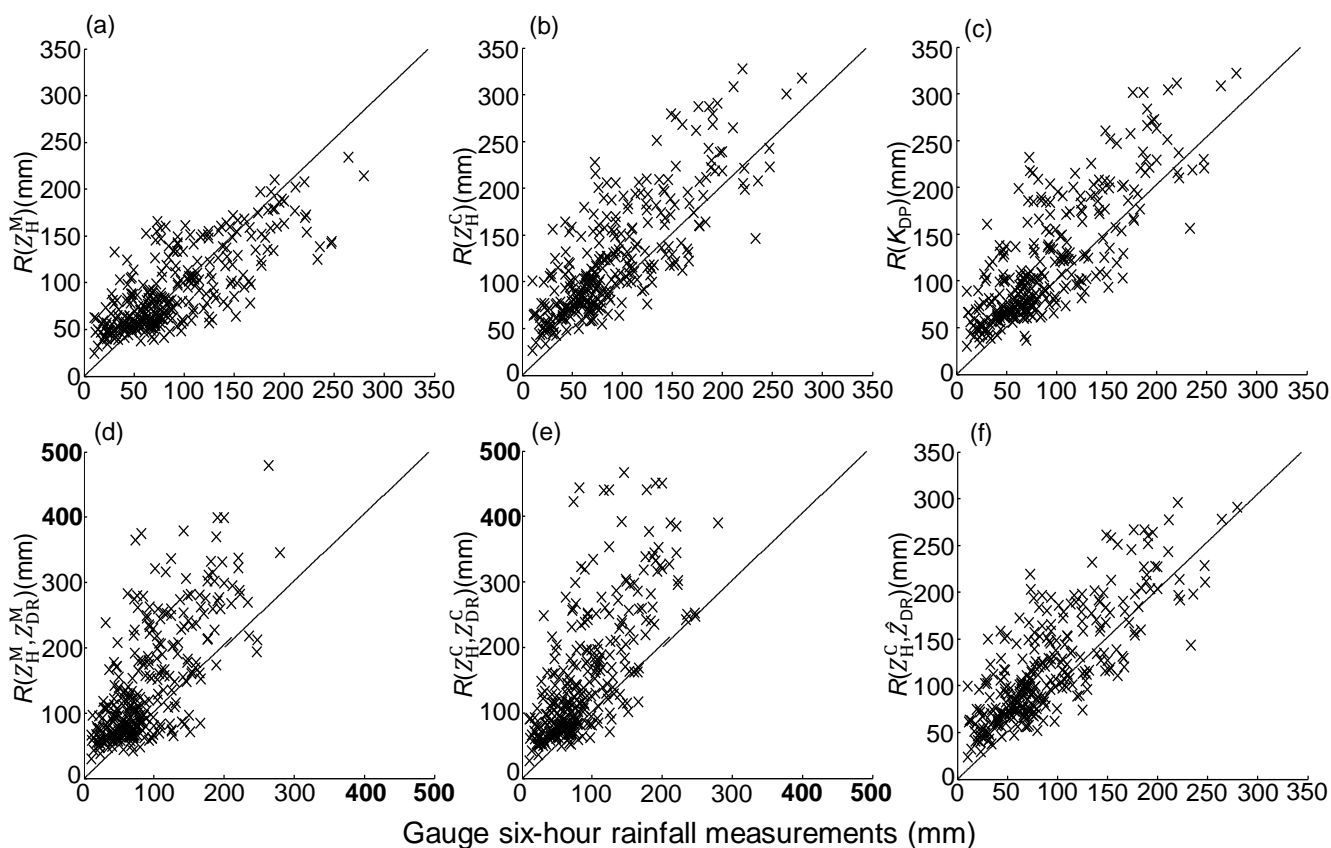
Fig. 16. The scattergram of six-hour rainfall estimates from radar versus corresponding gauge rainfall measurements. The radar rainfall estimates are derived at 2200 UTC 09 August 2019 using (a) $R(Z_H^M)$, (b) $R(Z_H^C)$, (c) $R(K_{DP})$, (d) $R(Z_H^M, Z_{DR}^M)$, (e) $R(Z_H^C, Z_{DR}^C)$, and (f) $R(Z_H^C, \hat{Z}_{DR})$.
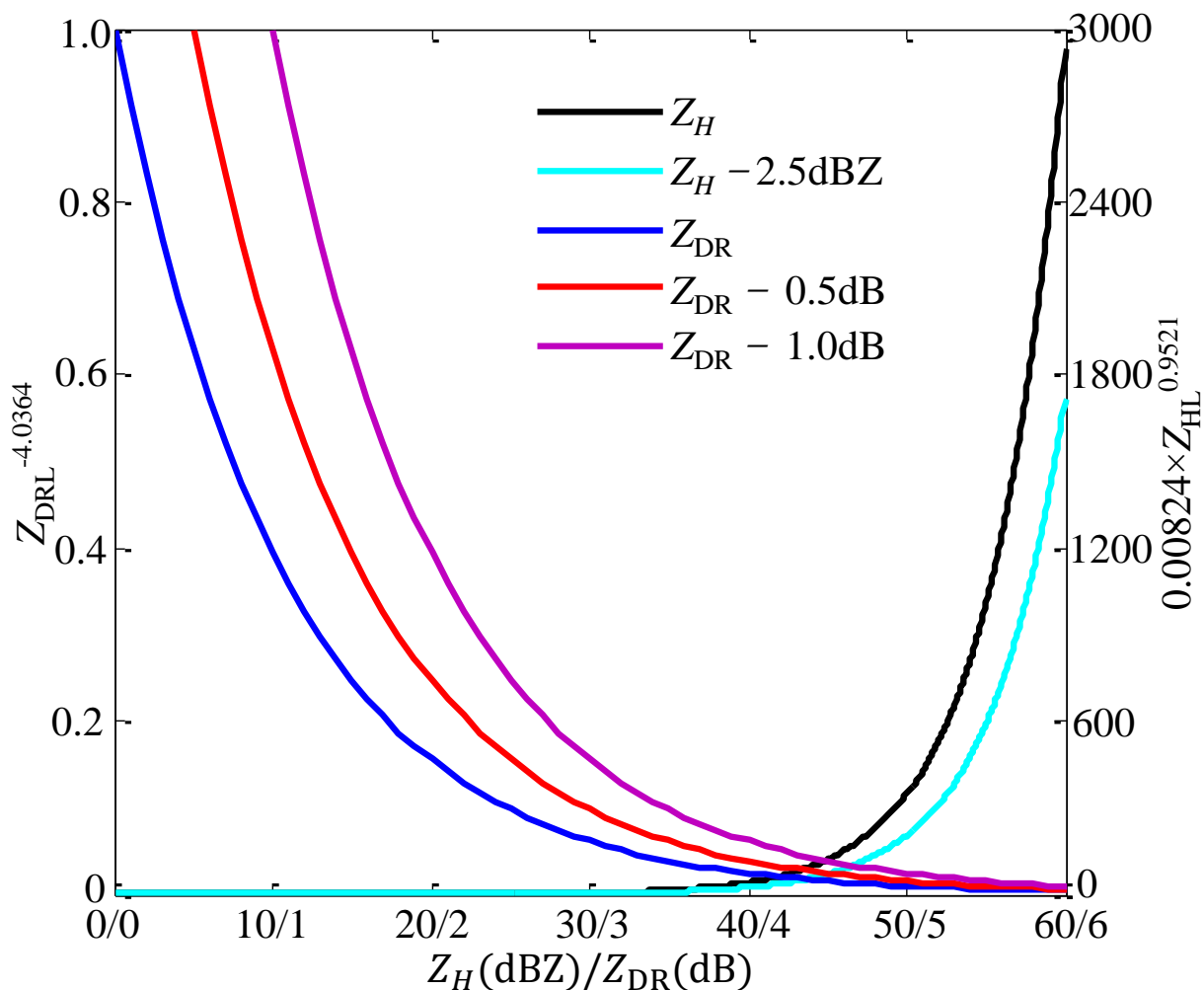
Fig. 17. The contribution of Z_H-related and Z_{DR}-related terms in $R(Z_H, Z_{DR})$ relationship with different Z_H and Z_{DR} biases. Z_{HL} and Z_{DRL} refer to Z_H and Z_{DR} at linear scale, respectively. The $R(Z_H, Z_{DR})$ relationship is detailed in Eq. 11c.